Structures 69 (2024) 107201

Contents lists available at ScienceDirect

Structures

journal homepage: www.elsevier.com/locate/structures

Failure-mechanism for wind turbines supported by pile groups at the Kugino wind farm in the Kumamoto earthquake

Lilin Wang [a,b,c], Takeshi Ishihara [c,*]

[a] Hainan Institute, Zhejiang University, Hainan, 572025
[b] Ocean College, Zhejiang University, Zhoushan 316021, PR China
[c] Department of Civil Engineering, School of Engineering, The University of Tokyo, 7-3-1, Hongo, Bunkyo-ku, Tokyo, Japan

ARTICLE INFO

Keywords:
Wind turbine
Pile group
Soil-footing interaction
Tower buckling
Kumamoto earthquake

ABSTRACT

The Kugino wind farm at Japan was seriously damaged in the severe Kumamoto earthquake, characterizing as all three pile group cracks but only one tower buckling. This study aims to reveal the failure mechanism underlying such damage pattern through the Beam on Nonlinear Winkler Foundation (BNWF) analyses, where the soil-footing interaction is considered with a new q-z model (QzSimple6). It identifies three parameters in a hyperbolic function to match any desired modulus reduction curve, whereas adjusts the unloading-reloading curves iteratively with the Ishihara-Yoshida rule to achieve site-specific soil damping curve. The QzSimple6-based BNWF analyses quantitatively reproduces centrifuge test results of a pile group foundation system, and newly reveals the soil-footing interaction does not influence pile bending moments but reduces the point mass acceleration. A parametric study is conducted on the full BNWF model with identifying pile group supported wind turbine, but with scaling soil stiffness and strength. The thrust force is attracted from the aero-elastic analysis in OpenFAST and the free-filed seismic displacement are calculated with the site response analysis in OpenSees. The simulation shows consistency with site observations that the No.2 wind turbine tower is destined to buckling at the height of around 13.9 m due to the sudden reduction of tower thickness, while No.1 and No.3 towers could remain safe potentially because soil properties under them are softer than that under the No.2 tower. In contrast, all three pile groups are found to be cracked under the Kumamoto earthquake intensity since the pile bending moment relies on the footing rigidity rather than the footing-soil interaction.

1. Introduction

Severe earthquakes led to damages of wind turbine towers and foundations in the last decades (Harukigaoka Wind Power [1], Butt and Ishihara [2], Wang and Ishihara [3]). These indicate the earthquake-induced damage needs to be considered in the design of wind turbine towers and foundations (see DNVGL [4]). To accurately evaluate the responses of wind turbine supporting structures, the soil-structure interaction shall be considered. JSCE guideline (Ishihara [5]) recommends two approaches to model the soil-structure interaction, being the equivalent linear one-dimensional (1D) method for the case with a maximum shear soil strain less than 1 % and the finite element (FE) method to consider the soil-structure interaction for cases with a maximum shear soil strain larger than 1 %, respectively. Due to model complexity, computational effort, and laborious data processing, the FE analysis may hardly be used to design wind turbines in a large wind farm with more than 100 wind turbines.

As the pile group consists of piles and footing, the soil-structure interaction of pile group includes the soil-pile interaction and the soil-footing interaction. In terms of modeling the soil-pile interaction, many well-known p-y models were proposed (see Zhang and Andersen [6], Wang et al. [7], Lai et al. [8], Zhang et al. [9]), Cheng et al. [10]), i.e., Cheng et al.[10] developed a novel cyclic p-y elastoplastic model based on the bounding surface theory, which can well capture the main cyclic characteristics of pile-head load-displacement curve, such as nonlinearity, hysteresis, displacement accumulation, and stiffness degradation. As summarized in Wang and Ishihara [11]; few previous hysteretic p-y models can capture the specific where damping becomes extremely important when it comes to seismic engineering where damping becomes extremely important. They also proposed a new hysteretic p-y model PySimple5 being capable of reproducing modulus reduction and damping curves. PySimple5 was validated by a series of

* Corresponding author.
E-mail address: ishihara@bridge.t.u-tokyo.ac.jp (T. Ishihara).

https://doi.org/10.1016/j.istruc.2024.107201
Received 7 April 2024; Received in revised form 14 July 2024; Accepted 27 August 2024

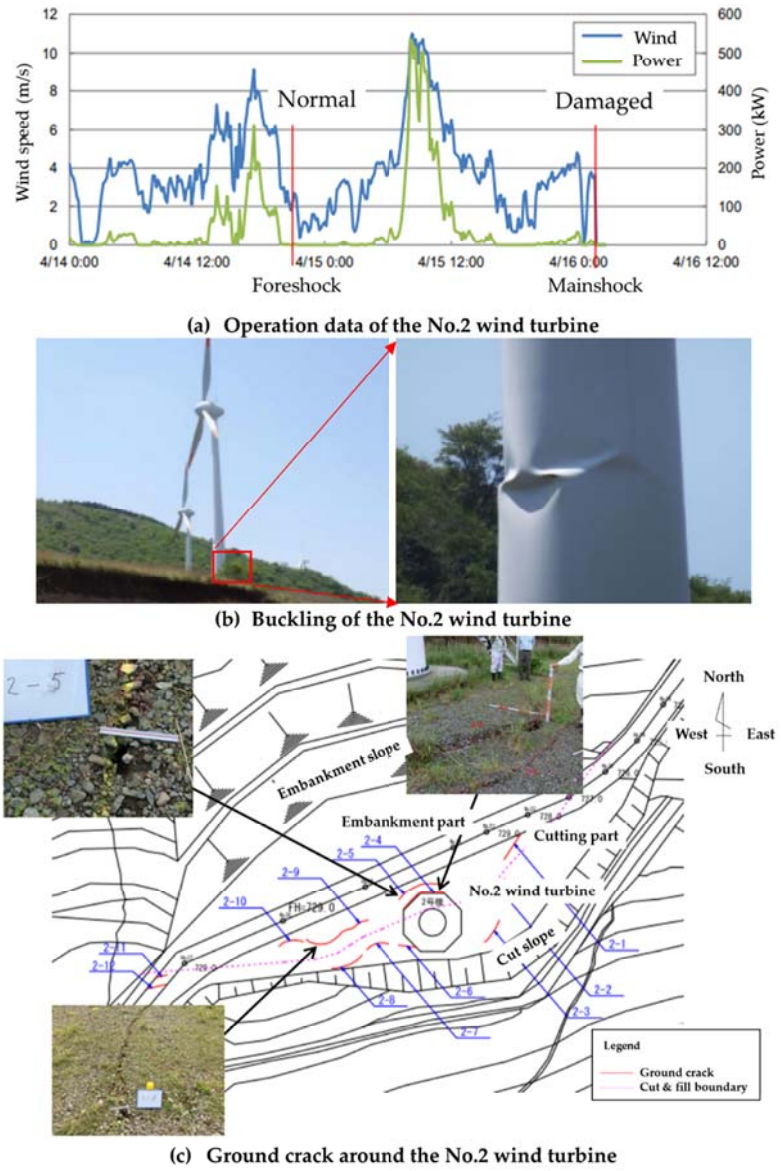

Fig. 1. Damages at the Kugino wind farm in Kumamoto earthquake (Harukigaoka Wind Power [1]).

centrifuge tests and well captured the superstructure acceleration and pile bending moment for all shear strain levels, while the conventional PySimple1 only suited the maximum soil shear strain less than 1 % and significantly underestimated the superstructure acceleration and pile bending moment when the maximum soil shear strain was 9.1 %. Regarding to the soil-footing interaction, the q-z model is needed. Raychowdhury and Hutchinson [12] recalibrated QzSimple1 by static and cyclic tests of shallow foundations and named it as QzSimple2, which can consider not only the material nonlinearity but also the geometrical nonlinearity. However, QzSimple2 failed to match the modulus reduction curve due to a large linear portion in the model. To improve the performance of QzSimple2. Wang and Ishihara [13] proposed the QzSimple4 model by replacing the elastoplastic component in QzSimple2 to yield a smooth modulus reduction curve. The material constant C in the model can control its backbone to match well with the desired modulus reduction curve. However, QzSimple4 still overestimates the damping value when a large deformation evolves. Although many other q-z models (e.g. Allotey and El Naggar [14–16]) were also proposed, according to the authors' best knowledge, there is no model that can reproduce the modulus reduction and damping curves at the same time.

The dynamic responses of wind turbine supporting structures have been investigated within a deterministic framework (e.g. Bazeos et al. [17], Witcher [18], Song et al. [19], Kim et al. [20], Wang and Ishihara [13], Liang et al. [21], Huang et al. [22], Alkhoury et al. [23]) and within a probabilistic framework (Kiyomiya et al. [24], Mensah et al. [25], P é rez Rocha et al. [26], Nuta et al. [27], Kim et al. [20], El Haj AK et al. [28]). Experimental tests (e.g. Prowell et al. [29]; Zhao et al. [30]) and field monitoring (Lauffer et al. [31], Adams et al. [32], Sim et al. [33], Cheng et al. [34], Cheng et al. [35], Wang et al. [36], Cheng et al. [37], Wang et al. [38], Wang et al. [39]) have also been carried out to predict the seismic loading of wind turbine supporting structures. Despite extensive research on this topic, the studies on the failure-mechanism of wind turbines in seismic hazards are very limited (Katsanos [40]). Wang and Ishihara [13] performed a parametric study to reveal the failure mechanism of shallow foundations at the Aso-nishihara wind farm caused by the Kumamoto earthquake. They found that the severe earthquake led to the uplifting of shallow foundation resting on stiff soil and increased the seismic loading on shallow foundations significantly compared with that estimated by the SR (Sway-Rocking) model. The uplifting of shallow foundation is the main reason why the damages at the Aso-nishihara wind farm occurred and

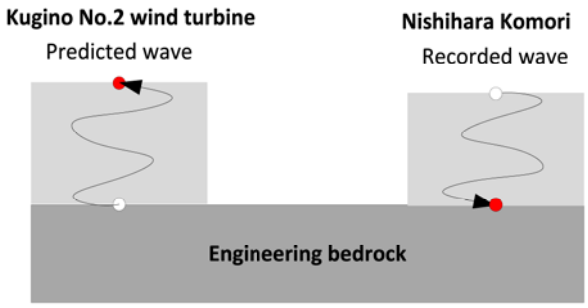

Fig. 2. Description of an approach to derive the seismic waves at the base of No.2 wind turbine.

shall be considered in the seismic design of shallow foundations. During the Kumamoto earthquake, severe failure also occurred at the Kugino wind farm, where one wind turbine tower was buckled and all the pile groups of three wind turbines were cracked. However, the failure mechanism is not yet clear.

Compared to the previous study, this study aims to (1) reveal the failure-mechanism of real pile group supported wind turbines, (2) adopt the integrated BNWF model with wind turbine blade, tower, footing, group piles, and p-y and t-z curves for soil-structure interaction, instead of a macro-element model for the foundation, (3) utilize the nonlinear soil reactions capturing the site-specific shear modulus reduction curve and damping curve, which forms the advance of this study. The failure for wind turbines at the Kugino wind farm suffered to the Kumamoto earthquake is described with overall damages, seismological aspects, wind turbines and foundations in Section 2. The BNWF model for wind turbines supported by pile groups at the Kugino wind farm is created with a newly developed q-z spring capable of reproducing site-specific modulus reduction and damping curves in Section 3. The dynamic loading is predicted for wind turbines at the Kugino wind farm suffered to the Kumamoto earthquake and the failure mechanism is clarified based on a parametric study in Section 4. Conclusions are summarized in Section 5.

2. Damage of the Kugino wind farm during Kumamoto earthquake

Overview of the damage in the Kugino wind farm and seismological aspects of Kumamoto earthquake are firstly described in Section 2.1. The structural properties of wind turbine and foundation are then summarized in Section 2.2.

2.1. Overview of the damage and seismological aspects of Kumamoto earthquake

The Kugino wind farm is in Minamiaso Village, Aso County, Kumamoto Prefecture and possesses three ENERCON E40 wind turbines supported by pile groups. Each wind turbine has a hub height of 46.25 m, a rotor diameter of 44 m and a rated power of 600 kW. The Kugino wind farm encountered serious damages in the Kumamoto earthquake in 2016 since the epicenter to the wind farm was only a 24 km distance. Fig. 1a shows the wind speeds and power outputs during the earthquake. Although the foreshock at 21:26 on April 14 erupted with a maximum magnitude of 7, no abnormalities were detected, and operation continued. The damage at the Kugino wind farm occurred at 01:25 on April 16 after the main shock broke out with a maximum seismic intensity of 7. The power system went out and all three wind turbines stopped operating. Fig. 1b and Fig. 1c illustrate the buckling of the No. 2 wind turbines and the ground cracks around the turbine, respectively. As a result, the pile group was cracked, and the tower was buckled at the height of 13.9 m. Unlike the No.2 wind turbine, the other two wind turbines experienced the crack of pile groups, but no buckling of the tower, which enlightens the necessity to make clear the failure mechanism.

Fig. 2 defines the approach to derive the seismic waves at the base of No.2 wind turbine from the recorded wave at the Nishihara Komori, where the seismic waves at the engineering bedrock are assumed the same for two sites [1]. After performing the site response analysis in OpenSees, Fig. 3a shows time-histories of three components of derived acceleration at the No.2 wind turbine site for the main-shock. To

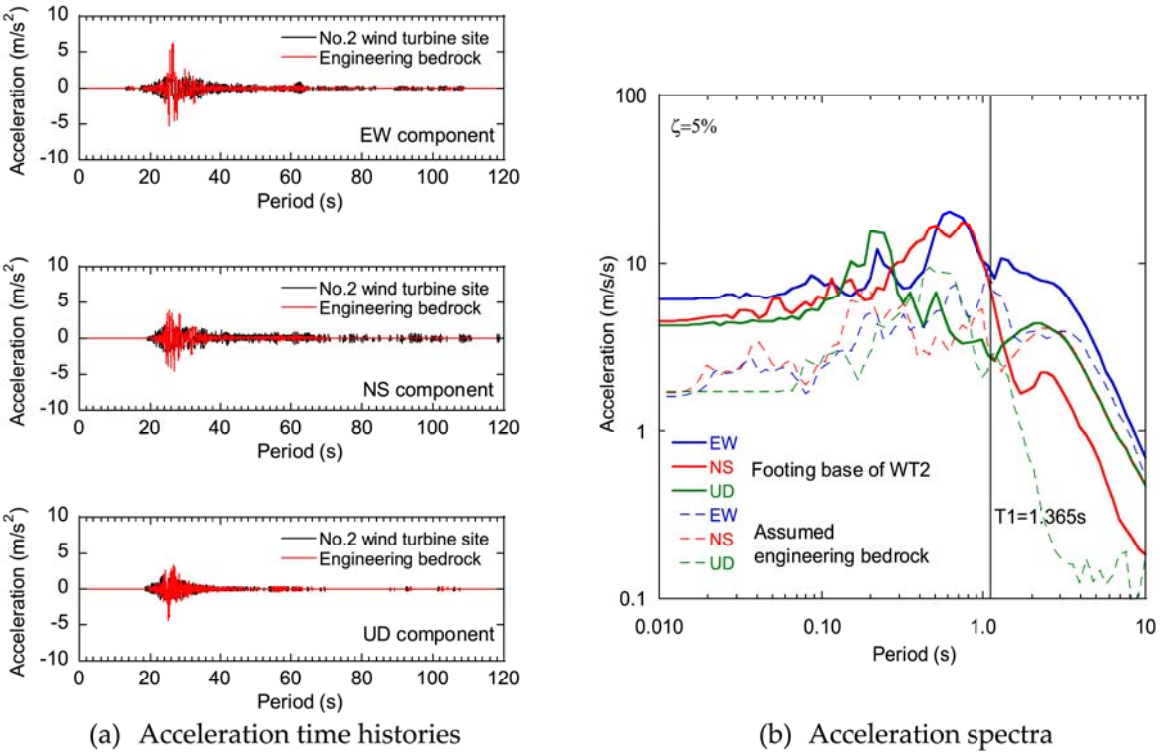

Fig. 3. Acceleration on the footing base and the engineering bedrock at No.2 wind turbine site.

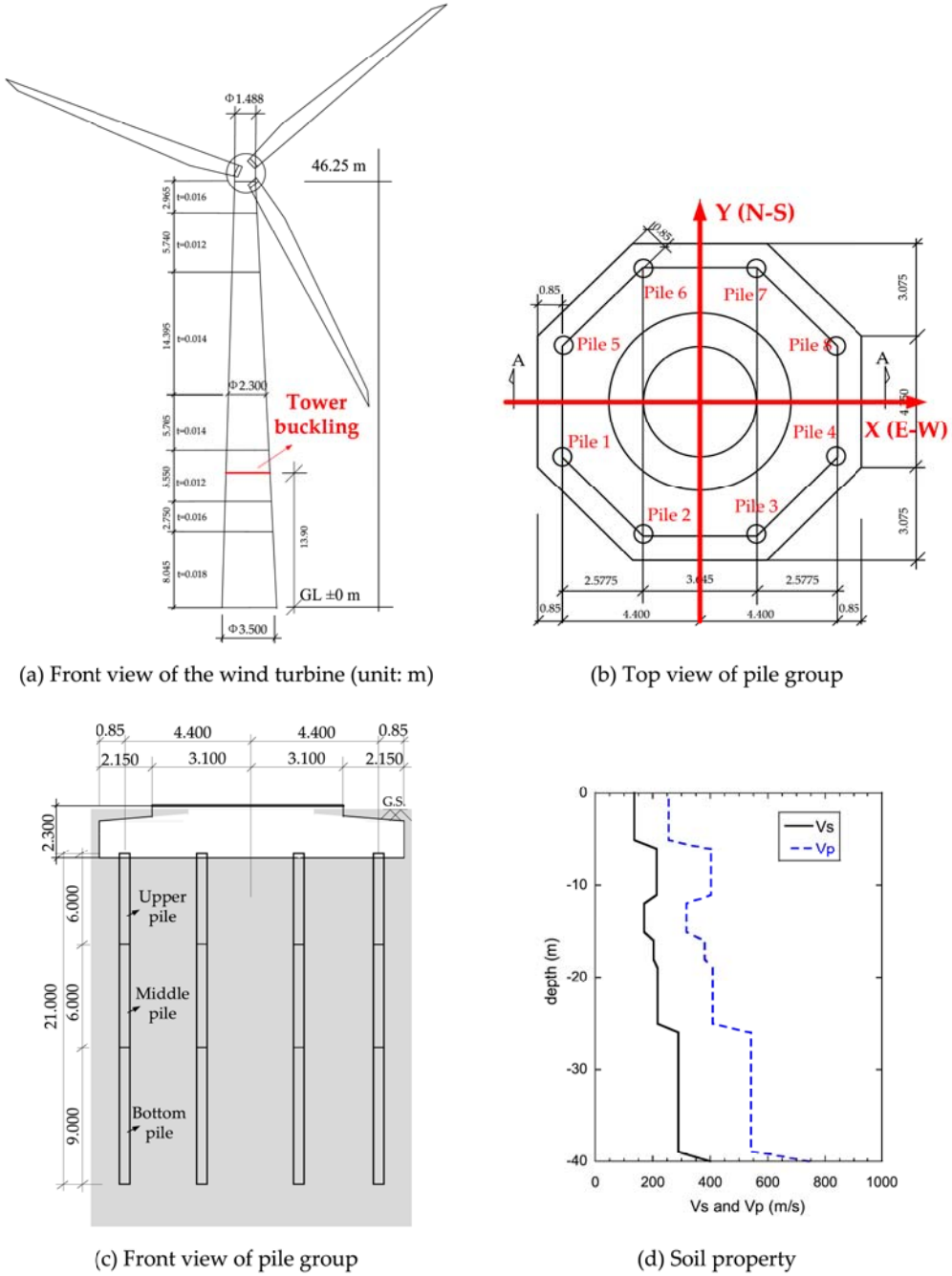

(a) Front view of the wind turbine (unit: m)

(b) Top view of pile group

(c) Front view of pile group

(d) Soil property

Fig. 4. Description of the No. 2 wind turbine and soil property at the site.

evaluate the spectral content of the derived ground motions at the No.2 wind turbine site, 5 %-damped response spectra are calculated and shown in Fig. 3b. The results for the wind turbine base are plotted with solid lines, while those for the engineering bedrock are p with broken lines. The comparison of the response spectra indicates that generally site amplification is significant for all three components and horizontal motions are amplified in almost all periods in the East-West direction and in a period range between 0 s (i.e. PGA) and about 1–2 s in the North-South direction, while vertical motions are significantly magnified at vibration periods less than 0.3 s or more than 1.5 s

2.2. *Description of wind turbine and foundation in the Kugino wind farm*

The No.2 wind turbine, with a rotor diameter of 44 m and a hub height of 46.25 m, is supported by a pile group foundation with 8 piles. The wind turbine tower is made of steel, whose diameter varies in the range of 3.500 m to 1.448 m from bottom to top. The thickness of wind turbine tower also varies in the range from 0.012 m to 0.018 m. However, the thickness does not reduce uniformly from bottom to top and a small thickness of 0.012 m exists in the height ranged from 10.795 m to 16.345 m. Each pile has a length of 21 m and a diameter of 0.6 m, which are made of three short piles, that is, a 6 m long SC pile in the top, a 6 m long PHC B pile in the middle and a 9 m long PHC A pile in the bottom. The eight piles are connected to an octagonal 2.3 m high steel-reinforced concrete footing. Both footing and piles are embedded in layered cinerites. The layered cinerites can be simplifed as a 18 m depth clay resting on a 22 m depth sand. The information of the No.2 wind tubrine is given in Fig. 4 and Table 1. Table 2 shows the soil stiffness, such as S-wave and P-wave velocities and strength, such as friction angle or cohesion at the site of the No. 2 wind turbine.

Table 1
Summary of the No.2 wind turbine.

Description	Value
Name	ENERCON E40
Rated power	600 kW
Hub height (above G.L)	46.25 m
Rotor diameter	44 m
Tower diameter, thickness	1.488–3.740 m, 0.012–0.018 m, see Fig. 4a
Nacelle and rotor mass	30,000 kg
Tower mass (with equipments)	43,484 kg
Footing shape, dimension	Octagonal, see Fig. 4b
Pile diameter, length and number	0.6 m, 21 m, 8
Foundation material	SC(Upper pile), PHC B (Middle pile), PHC A (Bottom pile), see Fig. 4c

The foundation is the only difference between the three wind turbines. The soil properties for the No.1 and No.3 wind turbines are modelled by scaling the soil properties of the No.2 wind turbine based on the geological survey and summarized in Table 3, which are used in a parametric study performed in Section 4 to reveal the failure mechanism of the No.2 wind turbine as given in Fig. 5. According to the JSCE guideline (Ishihara [5]), the modulus reduction and damping curves for the typical clay would be described using the H-D model with parameters of $\gamma_{0.5} = 0.15\%$, $h_{\max} = 17\%$, and those for the typical sand can be expressed using the H-D model with parameters of $\gamma_{0.5} = 0.1\%$, $h_{\max} = 21\%$. They are used for PySimple6 as explained in Section 3.2.

3. The BNWF model for wind turbines supported by pile groups at the Kugino wind farm

The BNWF model is built for the soil-structure interaction of pile group foundation in Section 3.1, in which the footing effects are evaluated using a new q-z model QzSimple6, while the pile group effects are captured by PySimple5 with group coefficients. The proposed QzSimple6 is presented in detail and compared with the conventional models in Section 3.2.

3.1. The BNWF model for the wind turbine supported by a pile group

The BNWF model of a wind turbine supported by a pile group is depicted in Fig. 6. The rotor-nacelle assembly is modeled by the standard lumped mass model (SLM model) with a dashpot at the hub height. The dashpot can also be replaced by a modal damping of 5 % approximately as given in Valamanesh and Myers [41]. The wind tubrine tower is modeled using the force-based beam-column element with an elastic section. Regarding to the footing, the ShellMITC4 shell element with the plate fiber section and the Elastic-Isotropic material is used. Fig. 7 shows the moment-curvature behavior of SC pile, PHCA pile, and PHC B pile corresponding to the maximum axial load N of 747.7 kN as shown in [1], for which the force-based beam-column elements with nonlinear sections and Multi-Linear material at 1.0 m intervals are adopted. All above elements are well defined in OpenSees (Mazzoni [42]).

The soil-pile group interaction is modeled via the Zero-Length element with PySimple5 and QzSimple6 to consider the pile group effects and the footing effects, respectively. The spring models of PySimple5 and QzSimple6 are newly developed and implemented in OpenSees. Detailed description of PySimple5 can be found in Wang and Ishihara [11], while that for QzSimple6 is stated in Section 3.2 in detail.

Table 3
Scaling factors used for the soil properties at the sites of No.1 and No.3 wind turbines.

Label	WT1	WT2	WT3
Scaling factor	0.75	1	0.8

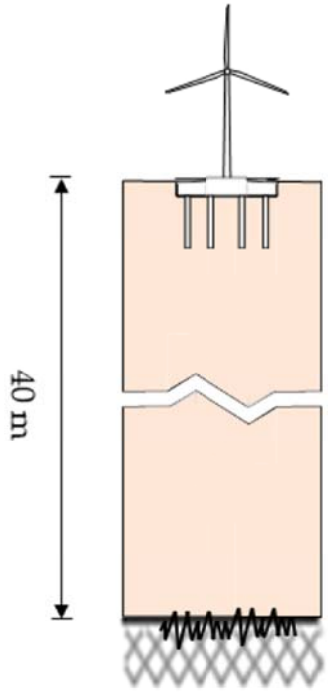

Fig. 5. Pile group supported wind turbines with different soil properties.

It is noted that when PySimple5 is applied to capture the interaction between soil and pile group, the pile group effects should be reflected into the parameters of ultimate capacity and initial stiffness. This study adopts the pile group coefficients as shown in Table 4 that is based on the centrifuge tests of a 3 × 3 pile group with a spacing-diameter ratio of 5 by Nguyen et al. [43].

3.2. A new q-z model QzSimple6

Wang and Ishihara [11] proposed PySimple5 capable of matching the site-specific modulus reduction curve and the desired damping curve. In this section, a new q-z model QzSimple6 is proposed following the same idea as PySimple5. As presented in Fig. 8, QzSimple6′s elastoplastic component can match the modulus reduction and damping curves and QzSimple6′s gap component can capture the uplifting behavior between soil and footing.

Eqs. (1)–(11) express the governing equations of QzSimple6. More specifically, the force and stiffness of linear component is shown in Eqs. (1)–(2), those of the hyperbolic component in Eqs. (3)–(4), those of the gap component in Eqs. (5)–(8), and those of the overall model in Eqs. (9)-(10). Eq. (11) shows the yielding function, in which C_r controls the elastic range of the proposed model. C_r equals to 0 in the proposed model, which means no pure elastic range exists in QzSimple6 as the linear and hyperbolic functions defines the plastic behavior of

Table 2
Soil properties at the site of the No. 2 wind turbine.

Type	Depth (m)	Unit weight (kN/m2)	Poisson ratio	Cohesion (kPa)	Friction angle (deg)	S-wave and P-wave velocity (m/s)
Clay	0~−18 m	17.0	0.3	20 −80	0	See Fig. 4d
Sand	−18 m~−40 m	19.0	0.3	0	42	

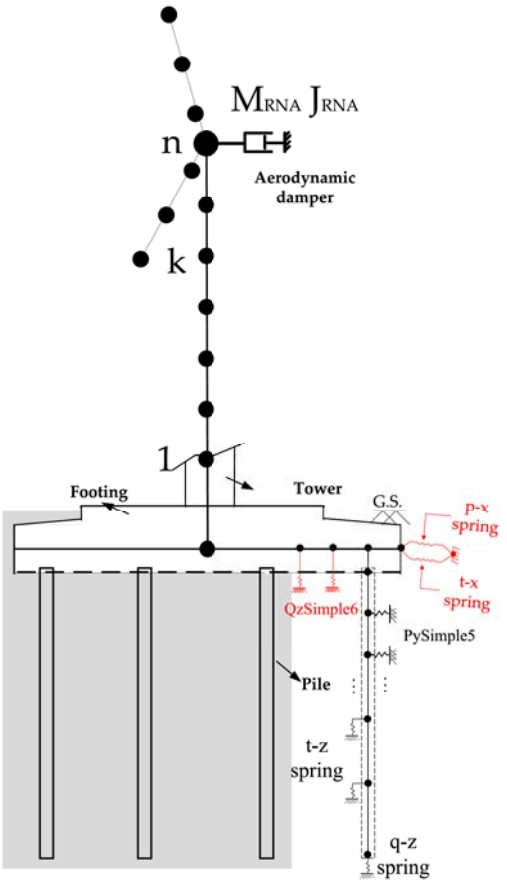

Fig. 6. Winkler model for the wind turbine supported by a pile group.

QzSimple6 together.

$$q^e = K^e z^e \tag{1}$$

$$K^e = \eta \frac{q_{ult}}{z_{50}} \tag{2}$$

$$q^p = B{\cdot}E{\cdot}q_{ult} - (B{\cdot}E{\cdot}q_{ult} - q_0)\left(\frac{A{\cdot}E{\cdot}c{\cdot}z_{50}}{A{\cdot}E{\cdot}c{\cdot}z_{50} + \left|z^p - z_0^p\right|}\right)^n \tag{3}$$

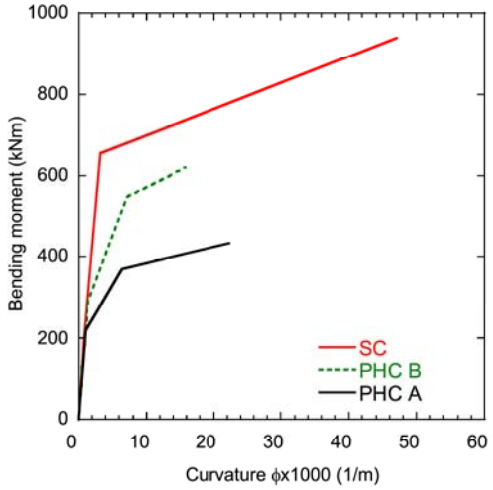

Fig. 7. The moment-curvature behvior of SC pile, PHC B pile and PHC A pile under maximum axial load.

Table 4
Group coefficients for a 3 × 3 pile group with a spacing-diameter ratio of 5 [22].

Pile type	Group coefficients of Ultimate bearing capacity (kN/m)	Group coefficients of Initial stiffness (kN/m^2)
Outer pile	0.766	0.656
Centre pile	0.728	0.592

Note that: the outer piles represent those piles are close to the footing side and the centre piles means the piles except the outer piles.

$$K^p = \frac{\partial q^p}{\partial z^p} = \frac{n{\cdot}sign(\dot{z})(B{\cdot}E{\cdot}q_{ult} - q_0)}{\left|z^p - z_0^p\right| + A{\cdot}E{\cdot}c{\cdot}z_{50}}\left[\left(\frac{A{\cdot}E{\cdot}c{\cdot}z_{50}}{\left|z^p - z_0^p\right| + A{\cdot}E{\cdot}c{\cdot}z_{50}}\right)^n\right] \tag{4}$$

$$q^g = q^s + q^c \tag{5}$$

$$q^s = C_s{\cdot}q_{ult} - \left(C_s{\cdot}q_{ult} - q_0^s\right)\left(\frac{z_{50}}{z_{50} + 2\left|z^g - z_0^g\right|}\right) \tag{6}$$

$$q^c = \begin{cases} 0.001\dfrac{q_u}{z_{50}} z_g \left(z_g > 0\right) \\ 1000\dfrac{q_u}{z_{50}} z_g \left(z_g \le 0\right) \end{cases} \tag{7}$$

$$K^g = \frac{\partial q^g}{\partial z^g} = \begin{cases} \dfrac{2n\left(q_0^s - C_s q_{ult}\right)}{z_{50} + 2\left|z^g - z_0^g\right|}\left(\dfrac{z_{50}}{z_{50} + 2\left|z^g - z_0^g\right|}\right) + 0.001\dfrac{q_u}{z_{50}}\left(z_g > 0\right) \\ \dfrac{2n\left(q_0^s - C_s q_{ult}\right)}{z_{50} + 2\left|z^g - z_0^g\right|}\left(\dfrac{z_{50}}{z_{50} + 2\left|z^g - z_0^g\right|}\right) + 1000\dfrac{q_u}{z_{50}}\left(z_g \le 0\right) \end{cases} \tag{8}$$

$$q = q^e = q^p = q^g \tag{9}$$

$$K = \left(1/K^e + 1/K^p + 1/K^g\right)^{-1} \tag{10}$$

$$f = \left|q - q_\alpha\right| - \left(C_r{\cdot}p_{ult}\right) \tag{11}$$

where q^e is the force in linear component, q^p is the force in hyperbolic component, K^e is the modulus of linear component, K^p is the modulus of hyperbolic component, K^g is the modulus of gap component and K is the combined modulus. $sign(\dot{z})$ is the sign function of $\dot{z}$ and $\dot{z}$ means the rate of z. f is the yield function, q_α is the value of q at the center of the elastic region (analogous to the backstress in the classical plasticity theory), $C_r{\cdot}q_{ult}$ is the yielding force and C_r is 0 in QzSimple6. q_0 is the value of q at the start of current plastic loading cycle and q_{ult} is the ultimate bearing capacity. z^e is the linear component of displacement, z^p is the hyperbolic component of displacement, z_0^p is the value of z_0 at the start of current plastic loading cycle and z_{50} is the displacement where $q = 0.5q_{ult}$. q^c and q^s are forces in the closure and the suction elements, respectively, q_0^s is the value of q^s at the start of current plastic loading cycle. z^g is the displacement across the gap element, z_0^g is the value of z^g at the start of current plastic loading cycle and C_s is the ratio of the maximum suction force to the ultimate bearing capacity. c, n and η define the shape of backbone curve, while A, B and E determine the shape of unloading and reloading.

The backbone curve relevant parameters (c, n, η) can be identified by GA and goal seeking using the criterion that the backbone curve shall be capable of matching the desired modulus reduction curve. The fitness function of GA, $1/RMSE$, is defined as the ratio of root mean squared error in Eq. (12), while the iteration will be stopped when Eq. (13) is satisfied, or the generation reaches 100.

$$RMSE = \sqrt{\frac{1}{N}\sum_{i=1}^{N}\left(\frac{K_i}{K_0} - \frac{G_i}{G_0}\right)^2} \tag{12}$$

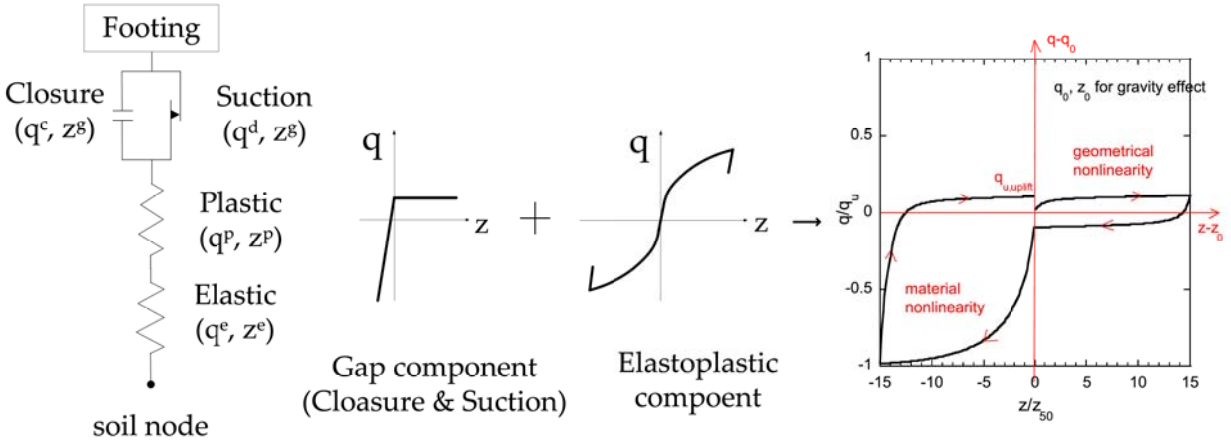

Fig. 8. Illustration of QzSimple6.

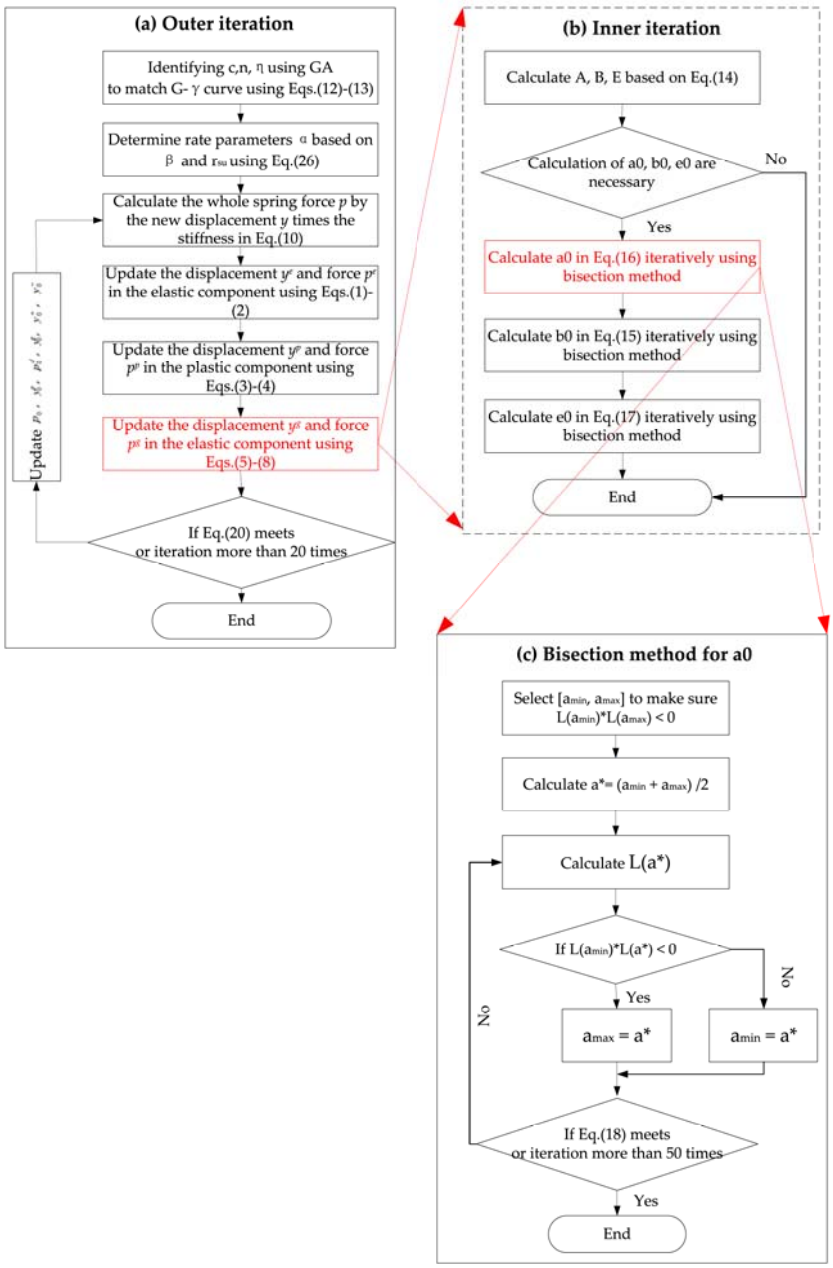

Fig. 9. Flow chart for determining the parameters in QzSimple6.

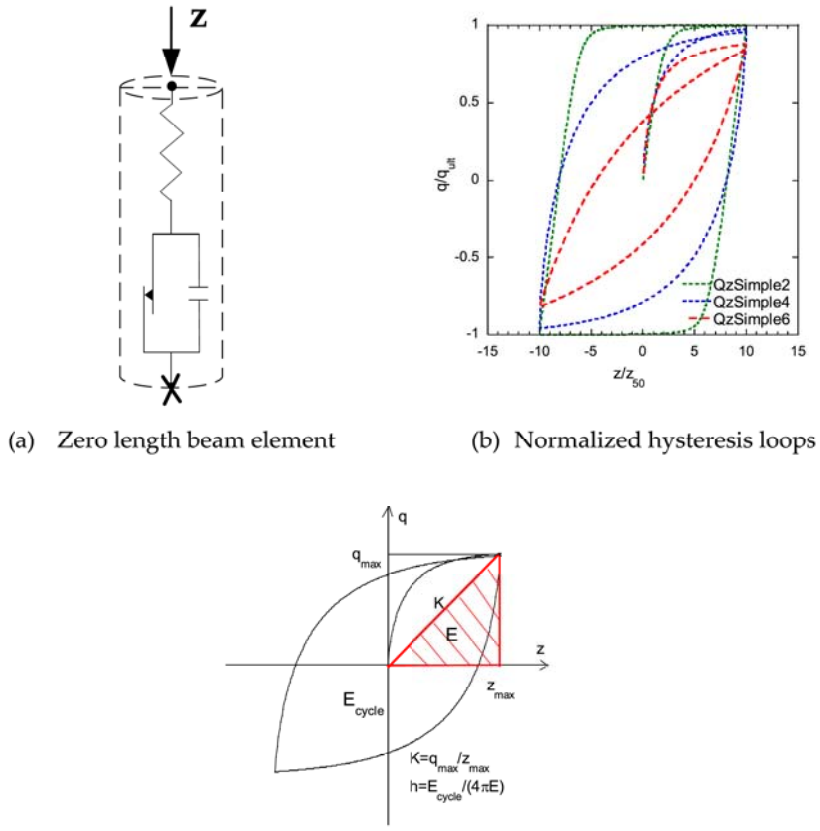

(a) Zero length beam element (b) Normalized hysteresis loops

(c) Derivation of stiffness and damping from hysteric loop

Fig. 10. Zero-Length beam element with QzSimple6 and normalized hysteresis loops.

$$RMSE \le 10^{-3} \quad \text{or} \quad \phi_j - \phi_{j-1} \le 10^{-3} \tag{13}$$

where $RMSE$ means the root mean square error. G_i is the modulus at the ith points of modulus reduction curve, while K_i is the corresponding stiffness of q-z curve. N is the number of points on the modulus reduction curve used for identification, which could be 10–20 uniformly distributed points on the modulus reduction curve. G_0 and K_0 are the initial shear modulus and stiffness, respectively. ϕ_j means the parameter at the jth generation and ϕ could be c, n and η.

The unloading-reloading relevant parameters (A, B and E) can be updated using the Ishihara-Yoshida rule (Ishihara et al. [44]) following the criterion that the backbone curve shall be capable of matching the damping curve. The Ishihara-Yoshida rule was proposed for the ground response analyses to solve the overestimation of soil damping when the soil strain is large. The same idea is used in this study for the q-z modeling. A, B and E have different values for different loading conditions as shown in Eq. (14) and are obtained iteratively to match the damping curve using Eqs. (15)-(17). It is noted that Eqs. (16)-(17) cannot be solved in a closed form for a_0 and e_0. They are solved numerically using the bisection method. The iteration will be stopped when Eq. (18) is satisfied, or the number of iterations reaches 50. Eq. (9) is also examined, and the iteration will be stopped when Eq. (19) is satisfied, or the number of iterations reaches 20.

$$\begin{cases} \text{skeletoncurve}: \ A = 1, B = 1, E = 1 \\ \text{unloading}: \ A = a_0, B = b_0, E = 1 \\ \text{reloading\&reunloading}: \ A = a_0, B = b_0, E = e_0 \end{cases} \tag{14}$$

$$b_0 = \frac{\left(\frac{c \cdot z_{50}}{c \cdot z_{50} + \left|z_0^p\right|}\right)^n - 1}{\left(\frac{a_0 \cdot c \cdot z_{50}}{a_0 \cdot c \cdot z_{50} + \left|z_0^p\right|}\right)^n - 1} \tag{15}$$

$$D\left(\frac{z_{0i}^p}{a_0}\right) = h\left(z_{0i}^p\right) \tag{16}$$

$$f\left(\frac{z_{0i}^p}{a_0}\right) = \frac{p_{0i}/b_0}{e_0} \tag{17}$$

Here, $h(y) = h_{\max}\left(\frac{z}{z_{50}+z}\right)$, $D(z) = \frac{1}{4\pi}\frac{\Delta W(z)}{W(z)}$,

$$W(z) = \frac{1}{2} z \cdot g(z), \ \ \Delta W(z) = 2\int_{-z}^{z} g(z_0) dz_0,$$

$$g(z) = \begin{cases} q_{ult} - (q_{ult} - q_{0i}/b_0)\left(\dfrac{c \cdot z_{50}}{c \cdot z_{50} + \left(z - z_{0i}^p/a_0\right)}\right)^n (\Delta z > 0) \\ -q_{ult} + (q_{ult} + q_{0i}/b_0)\left(\dfrac{c \cdot z_{50}}{c \cdot z_{50} - \left(z - z_{0i}^p/a_0\right)}\right)^n (\Delta z < 0) \end{cases}$$

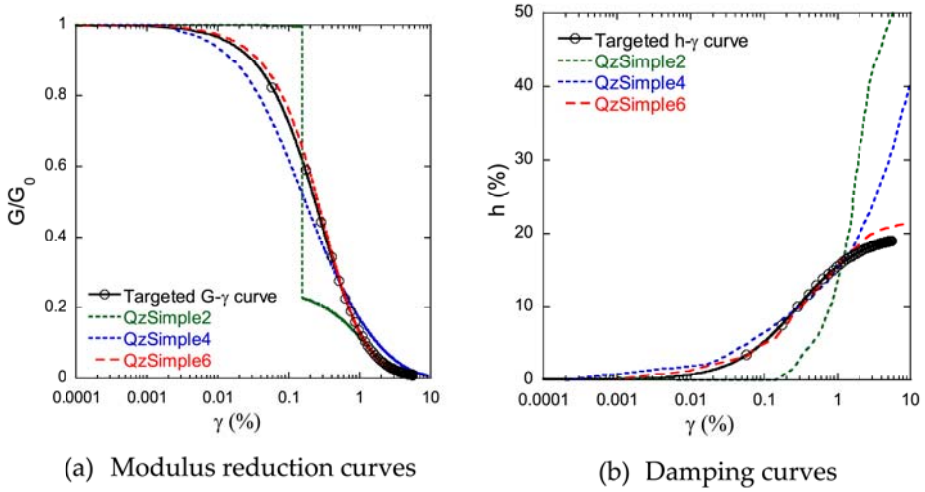

Fig. 11. Comparisons of modulus reduction and damping curves between QzSimple2, QzSimple4 and QzSimple6.

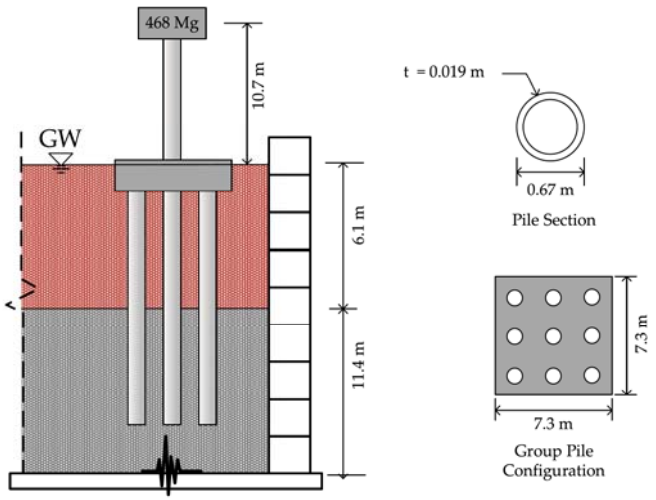

$$f(z)=\begin{cases} q_{ult}-\left(q_{ult}-\dfrac{q_{0i+1}/b_0}{e_0}\right)\left(\dfrac{c\cdot z_{50}}{c\cdot z_{50}+\left(\frac{z-z^p_{0i+1}/a_0}{e_0}\right)}\right)^n & (\Delta z>0) \\ -q_{ult}+\left(q_{ult}+\dfrac{q_{0i+1}/b_0}{e_0}\right)\left(\dfrac{c\cdot z_{50}}{c\cdot z_{50}-\left(\frac{z-z^p_{0i+1}/a_0}{e_0}\right)}\right)^n & (\Delta z<0) \end{cases}$$

where $h(z)$ is the desired damping curve. $D(z)$ represents the damping corresponds to the $q-z$ loops. $\Delta W(z)$ is the damping energy and $W(z)$ is the equivalent elastic strain energy. The coordinates $(z^p_{0i},\ q_{0i})$ and $(z^p_{0i+1},\ q_{0i+1})$ are the most recent two reversal points.

$$\text{abs}\left(D\left(\frac{z^p_{0i}}{a_0}\right)-h\left(z^p_{0i}\right)\right)\Big/h\left(z^p_{0i}\right)\le 1.0e^{-3}\ \text{ or }\ \text{abs}\left(D\left(\frac{z^p_{0i}}{a_0}\right)-h\left(z^p_{0i}\right)\right)\le 1.0e^{-3} \tag{18}$$

Fig. 12. Schematic of CSP5 test.

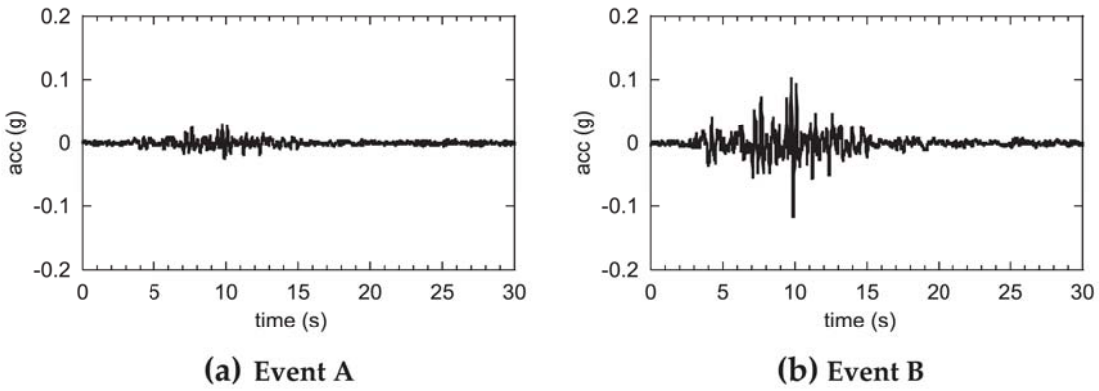

Fig. 13. Time histories of imposed acceleration in the centrifuged test CSP5.

Table 5
Soil parameters of CSP5 centrifuged test.

	clay (0-1.5 m)	clay (1.5-3 m)	clay (3-4.5 m)	clay (4.5-6 m)	sand
G_r (MPa)	0.5	1.3	1.8	2.4	41.5
B_r (MPa)	2.33	6.1	8.4	11.2	90.0
c_u (kPa)	2.5	6.5	9.0	12.0	0.0
ϕ (deg)	0.0	0.0	0.0	0.0	39.5

Note: G_r: low-strain shear modulus; B_r: low-strain bulk modulus; c_u: cohesion; ϕ soil friction angle.

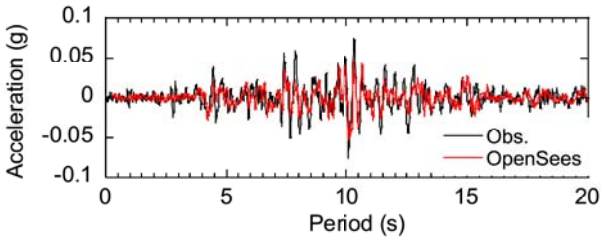

(a) Event A (γ_{max}=0.9%)

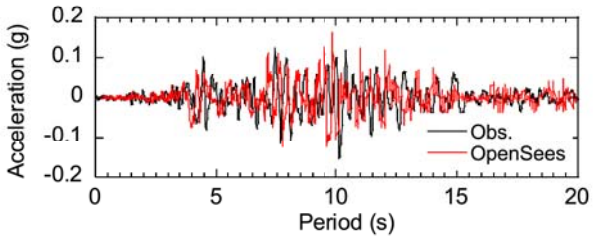

(b) Event B (γ_{max}=4.2%)

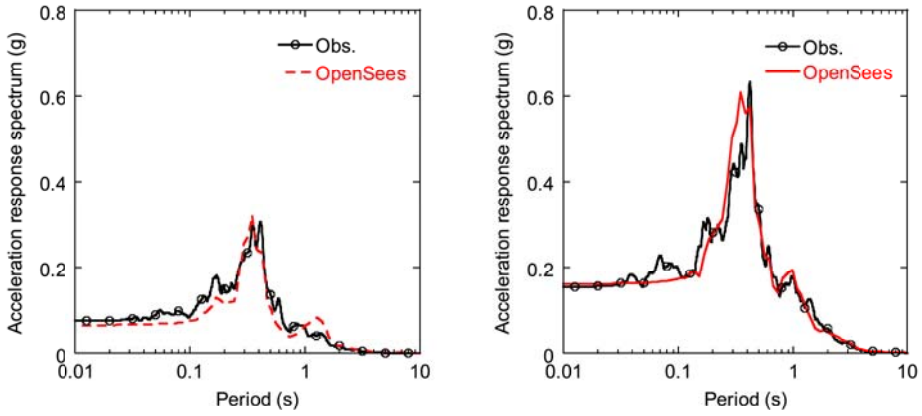

(c) Event A (γ_{max}=0.9%) (d) Event B (γ_{max}=4.2%)

Fig. 14. Comparison of measured and predicted acceleration time histories.

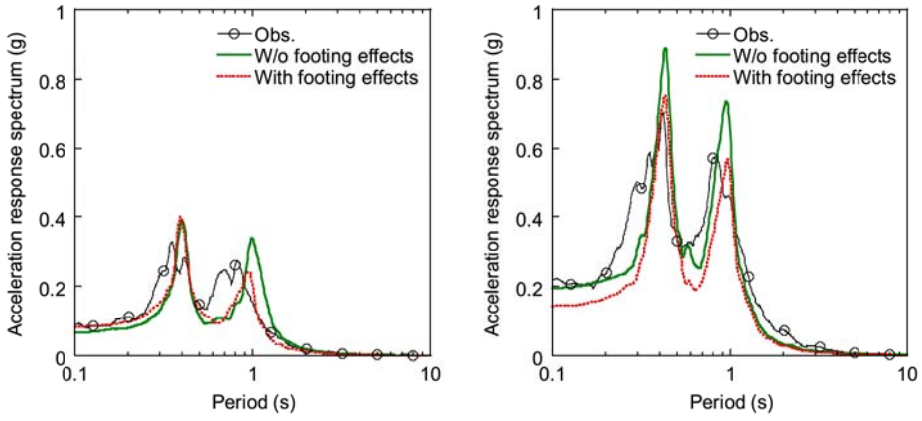

(a) Event A (γ_{max}=0.9%) (b) Event B (γ_{max}=4.2%)

Fig. 15. Comparison of measured and predicted acceleration response spectra of superstructure with the damping of 5 %.

$$\frac{3q - q^e - q^p - q^g}{q_{ult}} \leq 1.0e^{-12} \tag{19}$$

QzSimple6 is also implemented in OpenSees (Mazzoni [42]) and solved iteratively when it is applied to dynamic analyses of pile supported structures. The flow chart in Fig. 9 shows how QzSimple6 solved iteratively.

The performance of QzSimple6, QzSimple4 and QzSimple2 is compared in terms of whether matching the modulus reduction and

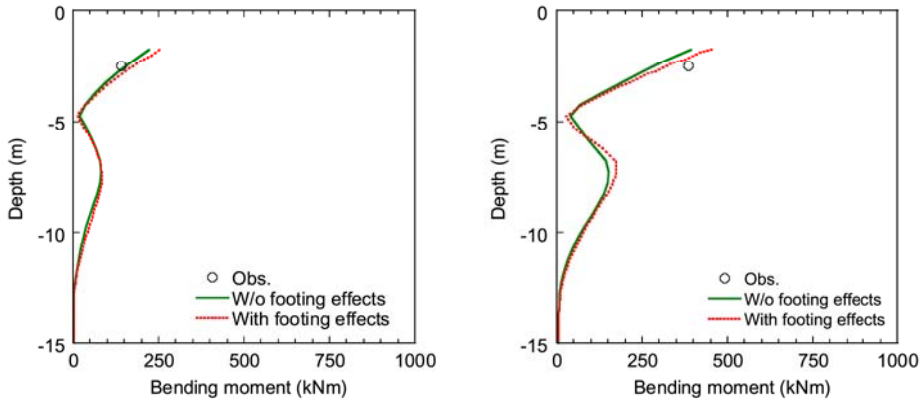

Fig. 16. Comparison of the measured and computed bending moment diagrams at the instance of maximum pile displacement.

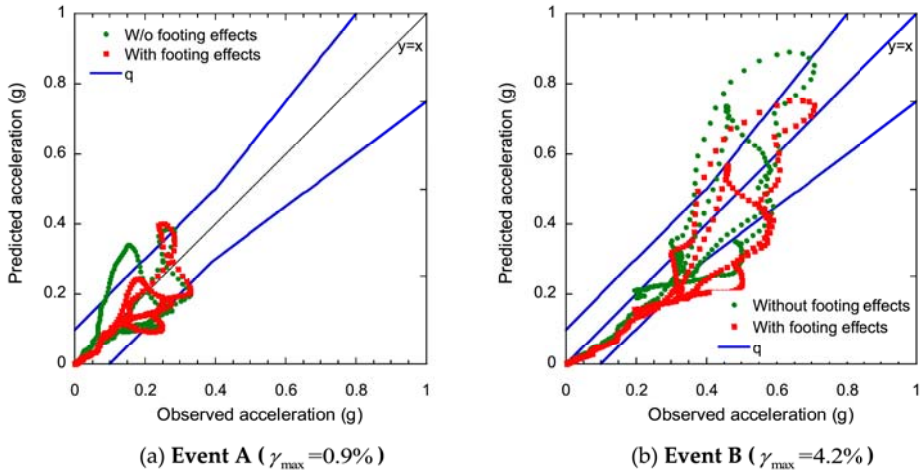

Fig. 17. Scatter plots for comparison between predicted and measured acceleration responses of superstructure with the damping of 5 %.

damping curves, for which the gap component shall be eliminated from QzSimple6, QzSimple4 and QzSimple2 to form a full hysteretic loop. With the input parameters (q_{ult} = 1, D = 1, C_s = 1, z_{50} = 0.473% calculated from $z_{50} = 2.5D\gamma_{0.5}/(1+\upsilon)$ and υ = 0.3), QzSimple6 is assigned to a Zero-Length beam element and subjected to a unit axial force cyclically as shown in Fig. 10a to fit the H-D model ($G/G_0 = 1/(1+\gamma/\gamma_{0.5})$ and $h = h_{max}\gamma/(\gamma_{0.5}+\gamma)$, $\gamma_{0.5}$ = 0.25%, h_{max} = 20%). The beam element is fixed at one node and free at the other node. Fig. 10b and 10c illustrate the load-displacement responses (also known as the hysteresis loop) and the definition of stiffness and damping based on the hysteresis loop, from which the modulus reduction and damping curves are derived and compared for QzSimple6, QzSimple4 and QzSimple2 in Fig. 11. QzSimple6 matches well with the target modulus reduction and damping curves while QzSimple2 fails to capture modulus reduction and damping curves. More specifically, QzSimple2 does not output a smooth modulus reduction curve due to the initial range of rigid behavior in the plastic component and it underestimates the soil damping at small strains, but significantly overestimates the soil damping at large strains. QzSimple4 outperforms QzSimple2 in terms of matching modulus reduction curve but is inferior to QzSimple6 when it comes to match the soil damping at large strains.

3.3. Validation of the BNWF model

The proposed model is validated by the centrifuge tests for a pile group in soft clay (referred as CSP5 Event A~B) (Wilson [45]). The CSP5 included not only a pile group but also a single pile. Since the CSP5 single pile results were simulated well by the PySimple5 model (Wang and Ishihara [11]), this section validates the QzSimple6 model using the CSP5 pile group results. As portrayed in Fig. 12, the pile group PG33 consisted of nine piles in a 3 × 3 grid whose pile cap was 7.3 × 7.3 m in plan, 2.3 m in thickness, and had a mass of 318 Mg. PG33 supported a superstructure mass of 468 Mg centered 10.7 m above the pile cap. Each pile was approximately equivalent to a 0.67-m diameter steel pipe pile with a 19 mm wall thickness. The soil profile in the CSP5 consists of a saturated soft clay layer with the thickness of 6.1 m and a saturated medium dense sand layer with the thickness of 11.4 m. As summarize in Table 3, the undrained shear strengths of the clay were 2.5, 6.5, 9.0 and 12.0 kPa for the depths of 0–1.5, 1.5–3.0, 3–4.5 and 4.5–6.0 m, respectively, while the friction angle of the sand equaled to 39.5^0. The effective unit weight was 7.75 kN/m^3 for clay and 9.81 kN/m^3 for sand, respectively. The excitations are imposed horizontally at the model base using the scaled Santa Cruz seismic waves with the amplitudes of 0.035 g for Event A and 0.12 g for Event B, which are shown in Fig. 13.

Following Wang and Ishihara [11], the modulus reduction and damping curves for clay is described using the H-D model with parameters of $\gamma_{0.5}$ = 0.15%, h_{max} = 17%, and those for sand using the H-D model with parameters of $\gamma_{0.5}$ = 0.1%, h_{max} = 21%. The seismic soil-pile interaction analysis includes the site response and pile response analyses. The site response analysis was performed in OpenSees using PressureIndependMultiYield material (PUDY) for clay and PressureDependMultiYield material (PMDY) for sand. From the predicted and

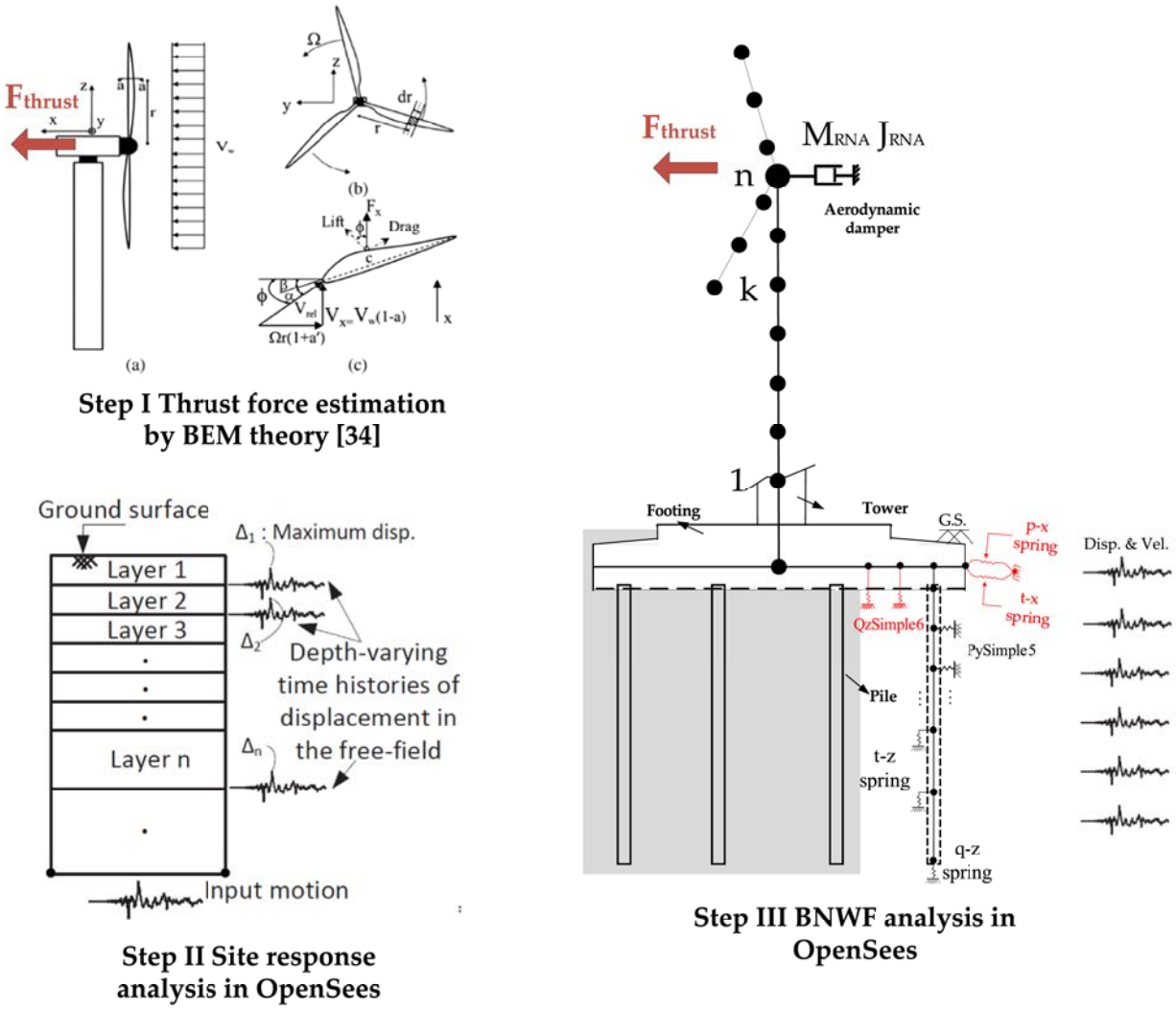

Fig. 18. Methodology for the BNWF analysis.

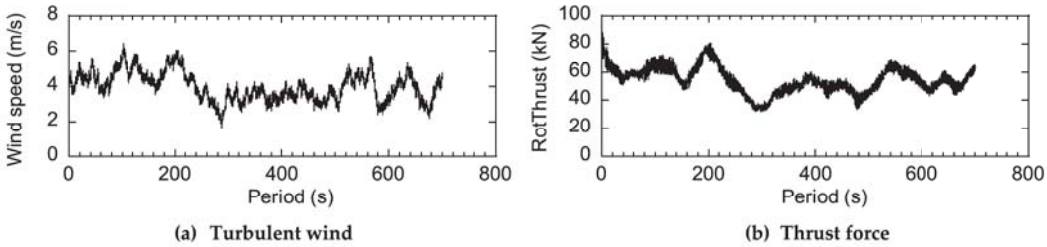

Fig. 19. Time histories of wind speed and thrust force.

measured acceleration responses illustrated in Fig. 14 at the depth of 1.6 m, it can be seen that the OpenSees simulations generally show reasonable agreement with measurements. More information about the site response analysis can be found in Wang and Ishihara [11].

The predicted responses of the superstructure and a side pile are presented in Fig. 15 and Fig. 16, respectively. The predictions with considering the footing effect agree well with measurements for both the superstructure and the pile group, though there is only one observed point for pile moments. Two peaks are observed for superstructure accelerations, one represents the dominant period of the excitation, while the other is for the natural period of the structure. The natural period of the structure is slightly overestimated probably due to that the group coefficient is not exactly derived for this experiment. The footing effect is shown of high importance to the superstructure acceleration for a pile group embedded in soft clay. Without considering the footing effect, the superstructure acceleration will be overestimated for all strain levels. This finding is consistent with the previous recognition in Tuner [46] that the superstructure response could be dominated by cap-soil interaction more than pile-soil interaction. Although there exists only one observation data of pile moment, the two predictions are close, implying that the footing effect exerts little influence on the pile bending moment as it relies more on the footing rigidity rather than the footing-soil interaction.

Fig. 17 plots the scatter plots for comparison between predictions and experiments for the acceleration responses of superstructure with the damping of 5 % and bending moments of pile shaft at the instance of

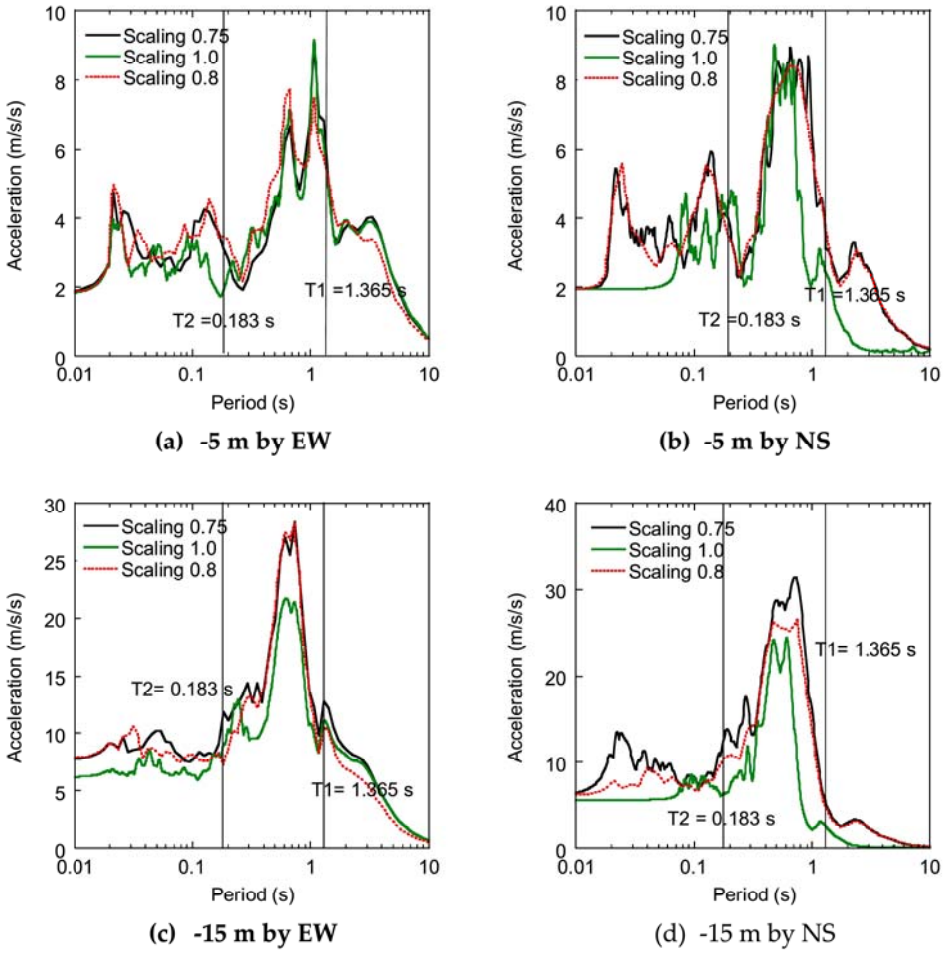

Fig. 20. Comparison of acceleration response spectra with the damping of 5 %.

maximum pile displacement, together with the corresponding validation metric boundary as shown in Appendix A. It is observed that better agreement is achieved for predictions with footing effects than those without footing effects. Since the footing effects exert little influence on the bending moments of pile, the validation metric for the pile moment is omitted here.

4. The dynamic loading prediction for wind turbines at the Kugino wind farm suffered to the Kumamoto earthquake

4.1. Methodology

As illustrated in Fig. 18, the dynamic loading is predicted through the BNWF analysis that incorporates three steps: (1) the time history of thrust force is estimated through performing the dynamic analysis in OpenFAST using an aero-elastic model with a fixed foundation; (2) Depth-varying time histories of displacement in the free-field are predicted by the site response analysis performed in OpenSees; (3) the dynamic loading on tower and piles are calculated via the BNWF analysis with the thrust force and the displacements obtained from previous two steps.

For the BNWF analysis, Rayleigh damping is applied for the structural damping with a damping ratio of 0.2 % for tower and 3 % for pile and footing. The structural damping ratio for the steel wind turbine tower shall be 0.2 % based on the filed measuremnt of a 2.4 MW gravity foundation supported wind tubrine (see Oh and Ishihara [47]). Since the piles are hollow piles, the structural damping ratio of 3 % seems reasonable. Although the footing is made of steel-reinforced concrete, it is quite rigid and the structural damping ratio of 3 % is applied. OpenSees defined its own methods for analysis. Constraint Handler determines how the constraint equations are enforced in the analysis; the numberer determines the mapping between equation numbers and degrees-of-freedom; the integrator determines the predictive step for time t + dt; the algorithm determines the sequence of steps taken to solve the non-linear equation at the current time step; the system specifies how to store and solve the system of equations in the analysis; the convergence determines when convergence has been achieved. More information can be found in Mazzoni et al. [42]. The analysis is conducted using the penalty method for the constraints handler, the reverse Cuthill-McKee scheme for the numberer, the displacement control method for the integrator, and the convergence tolerance on the energy unbalance in the system was 10^{-6}.

According to the JSCE guideline (Ishihara [5]), the criteria shown in Eq. (20) are adopted to evaluate the safety of tower under the strong earthquake.

$$\frac{\sigma}{f} = \left(\frac{\sigma_c}{f_{cr}} + \frac{\sigma_b}{f_{cr}}\right) + \left(\frac{\tau + \tau_T}{f_{cr}}\right)^2 \leq 1 \tag{20}$$

Here, $\sigma_c = N/A$, $\sigma_b = M/Z$, $\tau = 2Q/A$, $\tau_T = M_T/2\pi r^2 t$, $L = 4\sqrt{r \cdot t}$

$$
{}_{c}f_{cr} = \begin{cases} F\left(\dfrac{r}{t} \le 0.377\left(\dfrac{E}{F}\right)^{0.72}\right) \\ 0.6F + 0.4F\left(\dfrac{2.567 - r/t(F/E)^{0.72}}{2.190}\right)\left(0.377\left(\dfrac{E}{F}\right)^{0.72} \le \dfrac{r}{t} \le 2.567\left(\dfrac{E}{F}\right)^{0.72}\right); \\ 0.6E\dfrac{t}{r}\left\{1 - 0.901\left\{1 - \exp\left[-\dfrac{1}{16}\left(\dfrac{r}{t}\right)^{1/2}\right]\right\}\right\}\left(2.567\left(\dfrac{E}{F}\right)^{0.72} \le \dfrac{r}{t}\right) \end{cases}
$$

$$
{}_{b}f_{cr} = \begin{cases} F\left(\dfrac{r}{t} \le 0.274\left(\dfrac{E}{F}\right)^{0.78}\right) \\ 0.6F + 0.4F\left(\dfrac{2.106 - r/t(F/E)^{0.78}}{1.832}\right)\left(0.274\left(\dfrac{E}{F}\right)^{0.78} \le \dfrac{r}{t} \le 2.106\left(\dfrac{E}{F}\right)^{0.78}\right); \\ 0.6E\dfrac{t}{r}\left\{1 - 0.731\left\{1 - \exp\left[-\dfrac{1}{16}\left(\dfrac{r}{t}\right)^{1/2}\right]\right\}\right\}\left(2.106\left(\dfrac{E}{F}\right)^{0.78} \le \dfrac{r}{t}\right) \end{cases}
$$

$$
{}_{s}f_{cr} = \begin{cases} \dfrac{F}{\sqrt{3}}\left(\dfrac{r}{t} \le \dfrac{0.204(E/F)^{0.81}}{(l/r)^{0.4}}\right) \\ 0.6F + 0.4F\left(\dfrac{2.106 - r/t(F/E)^{0.78}}{1.832}\right)\left(\dfrac{0.204(E/F)^{0.81}}{(l/r)^{0.4}} \le \dfrac{r}{t} \le \dfrac{1.446(E/F)^{0.81}}{(l/r)^{0.4}}\right) \\ 0.8\dfrac{4.83E}{\left[l/r(r/t)^{1/2}\right]^2}\dfrac{t}{r}\left\{1 + 0.0239\left[\dfrac{l}{r}\left(\dfrac{r}{t}\right)^{1/2}\right]^3\right\}^{1/2}\left(\dfrac{1.446(E/F)^{0.81}}{(l/r)^{0.4}} \le \dfrac{r}{t}\right) \end{cases}
$$

where ${}_{c}f_{cr}$ is the allowable compression stress, ${}_{b}f_{cr}$ is the allowable bending stress, ${}_{s}f_{cr}$ is the allowable shear stress, N is the axial force, M is the bending moment, Q is the shear force, M_T is the torsional moment; A is the sectional area, Z is section factor, r is the sectional radius and t is the sectional thickness; E is Young's modulus and F is the yield value of axial force, shear force and moment.

4.2. Results and discussion

Fig. 1a reveals that at the start of the main shock of the Kumamoto earthquake, the No.2 wind turbine also encounters a wind speed of around 4 m/s. To approximate the thrust force at the hub height level, an aero-elastic wind turbine model is built in OpenFAST with a fixed foundation. The distributed properties of the blades in this study are scaled down from NREL 5 MW reference wind turbine (Jonkman et al., 2009) to generate the input file. This can result in a small deviation on the identified frequency of the blade modes but should have little or no influence on the frequency of fundamental FA tower mode. The overall mass, first mass moment of inertia, second mass moment of inertia, and nominal radial CM location of each blade are 3000 kg, 3.1E+ 4 kg m^2, 7.9E+ 5 kg m^2 and 6.0 m with respect to the blade root, respectively. Assumed the wind turbine is normally operated when earthquake occurs, the wind field is generated using the Turbsim with the Kaimal turbulence model and the B turbulence level. Wind speed is given at the hub height, and a power law, with a wind shear exponent of 0.2, gives the wind profile. The simulation of each load case lasts 700 s, and the results of the first 100 s will be removed to eliminate transient behavior. Fig. 19 plots the wind speed at the start of the main shock of the Kumamoto earthquake and the corresponding thrust force at the hub height, which would be applied to the tower top for the BNWF analysis. The thrust force could exert a maximum aerodynamic moment of 3.7E+ 3 kNm (80 kN * 46.25 m) at the tower base, which is negligible when compared to the maximum seismic moment of 2.5E+ 4 kNm as shown in Fig. 21.

The site response analyses for the parametric study are performed in OpenSees using PressureIndependMultiYield material (PUDY) for clay and PressureDependMultiYield material (PMDY) for sand, whose parameters are modified from those in Section 3.3. Fig. 20 compares the acceleration response spectra at depths of 5 m and 15 m in both EW and NS directions. Combined with the seismic wave at the engineering bedrock in Fig. 2, a general trend is found that the seismic wave is amplified at the deep depth and the amplification is reduced as the depth reduces. In light of varying soil properties, greater amplification is evolved by softer soil at deeper depths while that at shallower depths are mitigated. In summary, softer soils exert greater amplification.

Fig. 21a-21c plot the predicted maximum seismic loading on wind turbines towers including axial force, shear force and bending moment. The seismic loading is found to be increased along with the increase of soil stiffness, especially for the bending moment. Together with those given in Fig. 20, it can be concluded that although yielding larger amplification on seismic waves, the softer soil properties exert an overall reduction of the dynamic loading on tower as the soil springs are softened, which could be a potential reason why two left wind turbine towers (No.1 and No.3 wind turbines) remained safe. Assisted with Eq. (20), the stress ratio of wind turbine tower can be calculated and plotted in Fig. 21d. The stress ratio of No.2 wind turbine tower at the height of 13.9 m exceeds 1, which means the tower shall be buckled around this elevation. This is consistent with the buckling of No. 2 wind turbine around the height of 13.9 m. The reason why the stress ratio exceeds 1 at this elevation is that the sectional thickness is reduced here suddenly (see Fig. 4a). In terms of scaled soil properties, both stress ratios are less than 1, implying the integrity of the whole wind turbine after the Kumamoto earthquake. This may deduce the condition at the Kugino wind farm that the No.1 and No.3 wind turbines are supported in softer soils compared the No.2 wind turbine.

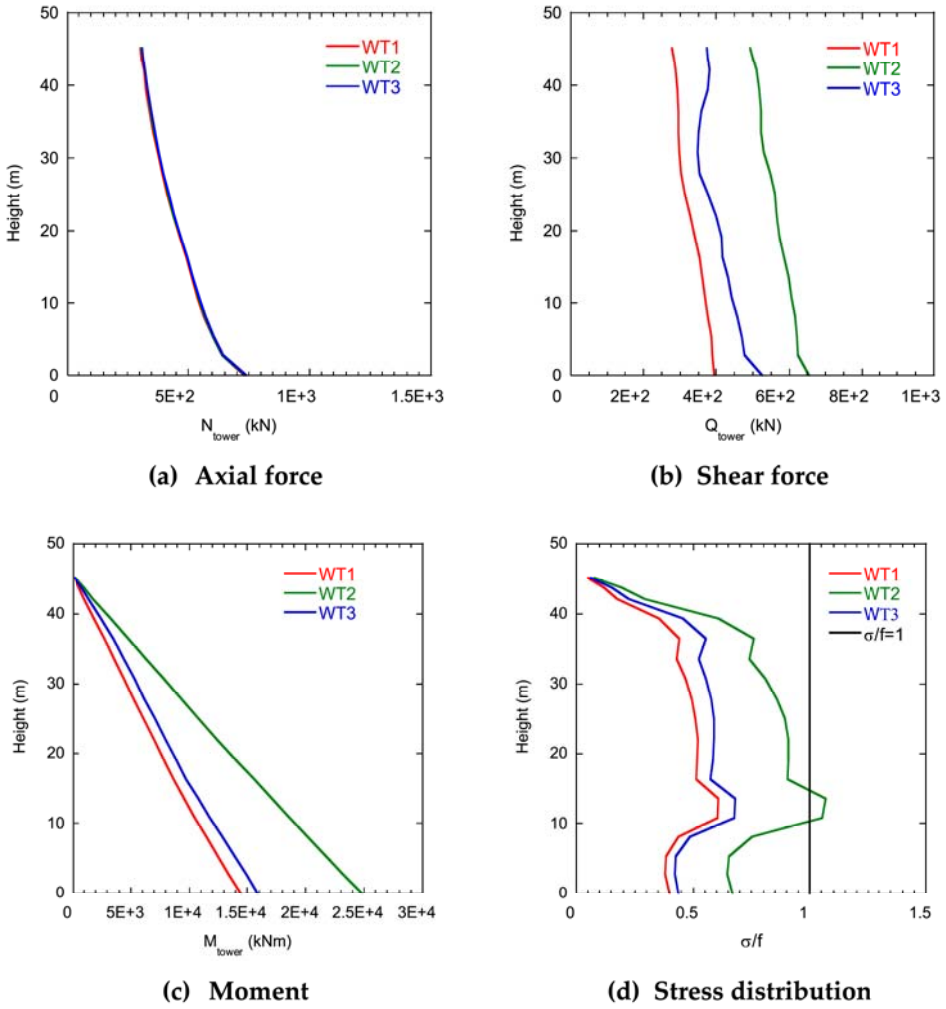

Fig. 21. Distribution of maximum seismic loading and stress.

The damage of pile group can be evaluated according to the pile design manual that is widely used for designing piles (Japan Road Association [48]). When the pile moment exceeds the yield moment (M_y), the pile would experience the third-level damage, while when the pile moment is beyond the ultimate moment (M_u), the pile behaves the fourth-level damage. The third-level or fourth-level damages were detected on piles for three wind turbines at the Kugino wind farm after the Kumamoto earthquake using the high-frequency impact elastic wave method (Nagai et al. [49]). Fig. 22a-22c show the predicted maximum axial force, shear force and bending moment on piles, based on which the bending moment normalized to the yield moment is plotted in Fig. 22d. The maximum bending moment on upper piles significantly exceeds the yield bending moment of piles by over two times, implying three wind turbine supporting piles was deemed to crack. These are consistent with the finding in accident survey after the Kumamoto earthquake. Similar to those observed in Section 3.3, the soil properties are found to exert little influence on the pile bending moment due to the pile bending moment relying more on the footing rigidity rather than the footing-soil interaction.

5. Summary and conclusion

This paper investigates the failure-mechanism for wind turbines supported by pile groups at the Kugino wind farm in the Kumamoto earthquake based on the Beam on Nonlinear Winkler Foundation (BNWF) analyses. A parametric study is performed using the same wind turbine with scaling soil stiffness and strength to make clear the failure mechanism why only the tower of No.2 wind turbine was buckled but all three piled foundations were damaged at the Kugino wind farm in the Kumamoto earthquake. The result and finding are summarized as follows:

(1) A new q-z model called QzSimple6 is proposed to model soil-footing interaction, being matched the desired modulus reduction curve by identifying three parameters in a hyperbolic function and the desired damping curve by applying the Ishihara-Yoshida rule that controls the unloading-reloading curves iteratively through three parameters.
(2) Though predicting the centrifuge test results of a point mass supported by a pile group, it is found that accelerations of the point mass are largely overestimated without considering footing effects, while bending moments of the pile group are almost not affected much by the footing effects.
(3) The No.2 wind turbine tower is destined to buckling at the height of around 13.9 m due to the sudden reduction of tower thickness, which is consistent with the real phenomenon observed during the Kumamoto earthquake.
(4) Although yielding larger amplification on seismic waves, the softer soil properties exert an overall reduction of the dynamic loading on tower as the soil springs are softened, which could be a potential reason why No.1 and No.3 wind turbine towers remained safe.
(5) In contrast, varying soil properties exerts little impact on the dynamic loading of pile groups as they were constrained by the

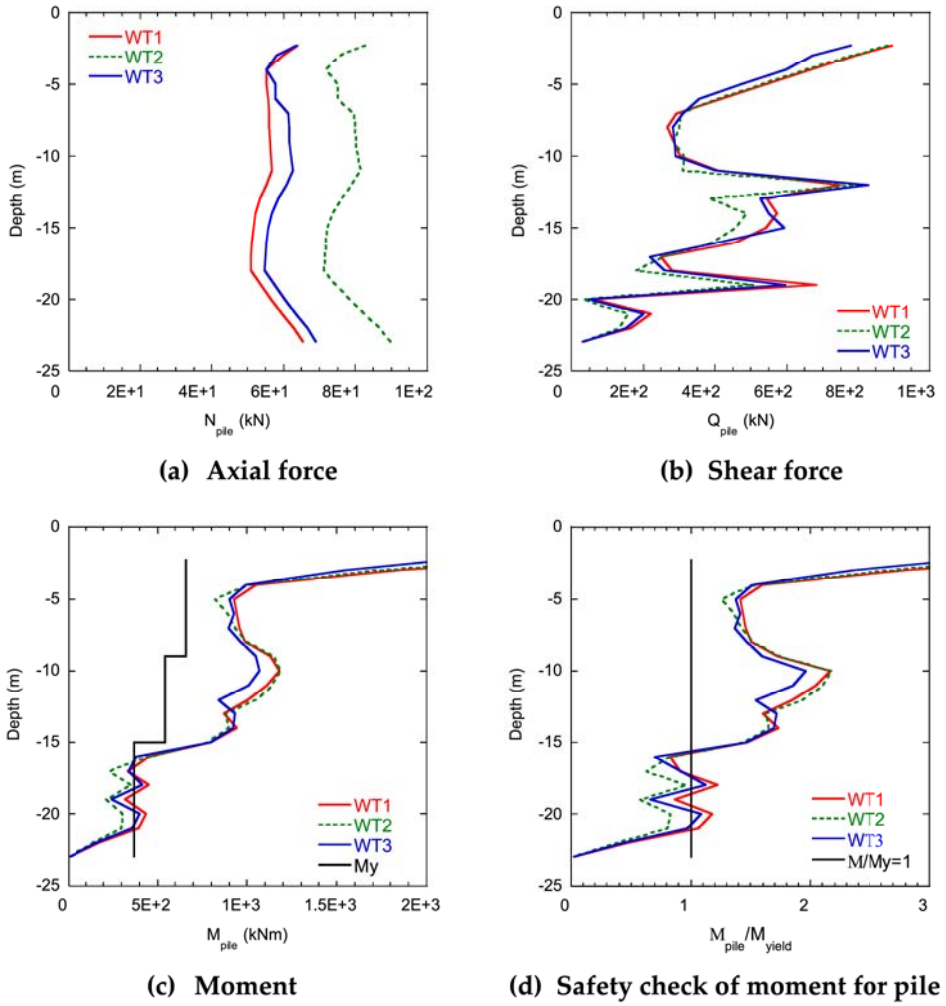

Fig. 22. Distribution of maximum seismic loading and stress of pile.

heavy footing. That's why all three pile groups were cracked in the severe Kumamoto earthquake intensity.

This paper focuses on the dynamic analyses of single wind turbine, a farm-level integrated dynamic analyses would be performed to investigate the damage thoroughly in the future.

CRediT authorship contribution statement

Lilin Wang: Writing – original draft, Visualization, Validation, Software, Methodology, Investigation, Formal analysis, Data curation, Conceptualization. **Takeshi Ishihara:** Writing – review & editing, Supervision, Project administration, Methodology, Funding acquisition, Conceptualization.

Declaration of Competing Interest

We declare that we do not have any commercial or associative interest that represents a conflict of interest in connection with the work submitted.

Acknowledgement

This research was carried out as part of a joint program funded by J-POWER, Shimizu Corporation, Toshiba Energy Systems & Solutions Corporation, MHI Vestas Offshore Wind Japan and ClassNK. The authors express their deepest gratitude to the concerned parties for their assistance during this study.

Appendix A. Validation of QzSimple6 by the shaking table test of a bridge pier-shallow foundation system

QzSimple6 is validated using a series of shaking table tests of a bridge pier-shallow foundation system under the seismic shaking (see Anastasopoulos et al. [50,51]). As illustrated in Fig. A1, the bridge pier-shallow foundation system (Table A1) rested on the dense dry sand (Table A2) were excited by sinusoidal accelerations.

A BNWF analysis is performed using QzSimple6. The column and footing are modeled using elastic beam-column elements, while the bridge deck is taken as a lumped mass. With 20 elastic beam-column elements to model the footing, 21 q-z springs are needed to capture the vertical soil-footing interaction. The q-z springs are modeled using Zero-Length elements with the uniaxial material QzSimple6. Input excitations are imposed using the Multi-Support pattern command to yield the absolute values of dynamic responses. The Rayleigh damping model is adopted to capture the structural damping. Following Wang and Ishihara [52], a common value of 0.2 % for the material damping of steel is adopted since the experimental models are made of steel. To compare, the simulations with QzSimple2 are also performed.

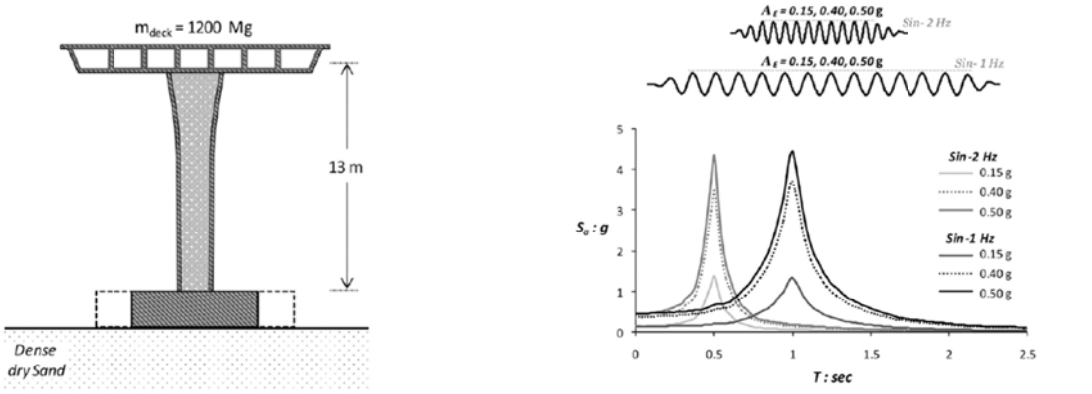

(a) **Bridge pier on shallow foundation of varying dimensions (in prototype)**

(b) **Representative acceleration time histories and their elastic response spectra**

Fig. A1. Bridge pier-foundation system and excitation inputs.

Table A1
Properties of large and medium foundations (in prototype).

Property	Large Foundation	Medium Foundation
Bridge deck mass [M (Mg)]	1200	1200
Pier height [H (m)]	13.6	13.6
Column height [hp (m)]	13.0	13.0
Column section area [A (m2)]	1.06	1.06
Column section moment of inertia [Ix (m4)]	0.32	0.32
Foundation length [L (m)]	11.0	7.0
Foundation width [B (m)]	1.7	1.4
Foundation height [H_f (m)]	0.6	0.6
Total vertical load (N (kN))	14362	13593
Static safety factor (FSv)	7.49	3.41
Fixed base period [T_0 (s)]	0.16	0.16

Table A2
Summary of soil properties in the shaking table tests.

Name	Longstone sand
Relative density Dr (%)	85
Specific weight Gs	2.64
Friction angle (deg)	44
Poisson ratio	0.25
Coefficient of friction	0.7

Figs. A1 and A2 depict the dynamic responses of bridge deck and footing under the base excitation of a 12-cycle 2-Hz sine pulse with the amplitude of 0.15 g and 0.50 g, respectively. Through the ascending slope of the rotation-settlement response, it is noticed that the footing is uplifted for the amplitude of 0.50 g but not for 0.15 g. Hence, the dynamic responses under the amplitude of 0.15 g are determined by the soil material nonlinearity (the elastoplastic component), while those for 0.5 g are controlled by the geometrical nonlinearity (the gap component). Incorporated with the site-specific modulus reduction and damping curves and an advanced gap model, QzSimple6 predicts the superstructure acceleration and foundation settlement for both small and large amplitudes. In contrast, QzSimple2 significantly underestimates the superstructure acceleration, indicating the importance of matching site-specific modulus reduction and damping curves.

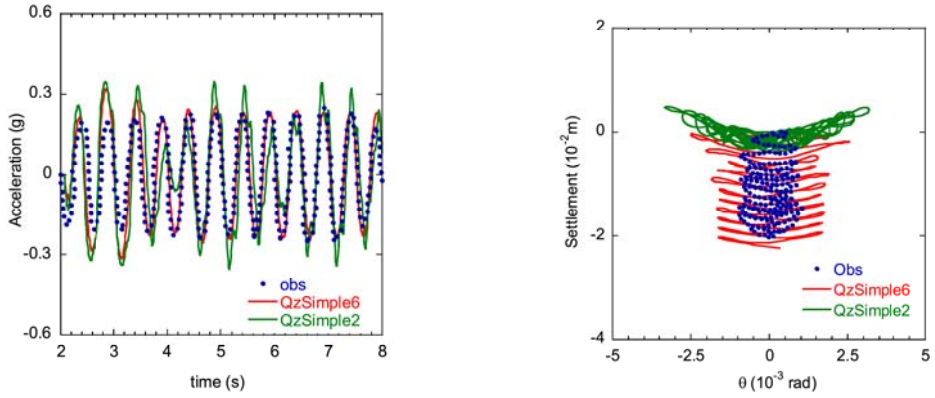

(a) Acceleration response of bridge deck **(b) Settlement-rotation response of foundation**

Fig. A2. Comparison of the responses predicted by QzSimple6 and QzSimple2 for the amplitude of 0.15 g.

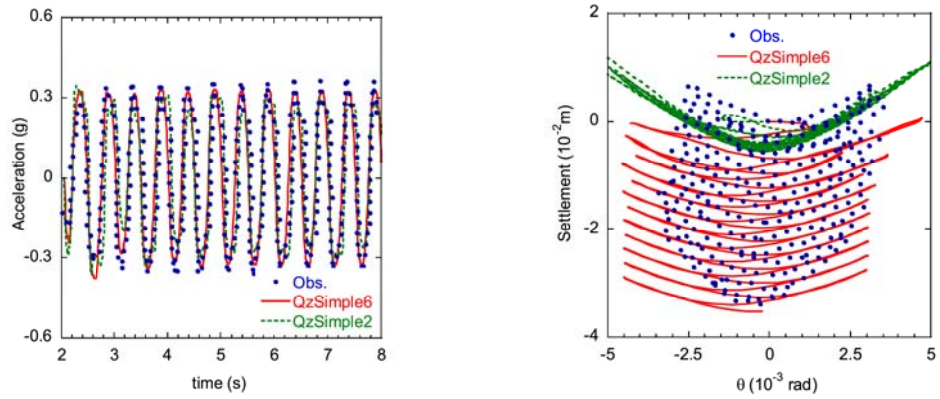

(a) Acceleration response of bridge deck **(b) Settlement-rotation response of foundation**

Fig. A3. Comparison of the responses predicted by QzSimple6 and QzSimple2 for the amplitude of 0.50 g.

A hit rate q is defined as the validation metric is defined to quantify the agreement between experiments and the proposed model (Schatzmann et al. [53] and Oettl [54]) as presented in Eq. (A1).

$$q = \frac{1}{N}\sum_{i=1}^{N} n_i, \quad \text{with} \quad n_i = \begin{cases} 1, & \left|\frac{y_i - x_i}{x_i}\right| \le D_q \ \text{ or } \ |y_i - x_i| \le W_q \\ 0, & \text{else} \end{cases} \tag{A1}$$

where x_i and y_i are the responses of bridge deck and footing from experiments and predictions, respectively. The data are picked corresponding to time points between 2 s and 8 s at 0.1-s intervals for the superstructure. For the footing, the rotations of 0 rad, −0.5E-3 rad and 0.5E+ 3 rad for the 0.15 g acceleration amplitude or those of 0 rad, −1.5E-3 rad and 1.5E+ 3 rad for the 0.50 g acceleration amplitude are selected. N represents the number of data, whileD_q and W_q are the threshold. Values of the metric corresponding to the complete agreement and disagreement are $q = 1$ and $q = 0$ respectively. The thresholds $D_q = 0.25$ and $W_q = 0.1|\max|$ are usually adopted, in which $|\max|$ is the maximum value of the observation. The scatter plots between predictions and experiments are compared in Figs. A4 and A5 for responses under the amplitudes of 0.15 g and 0.5 g, from which QzSimple6 is found to perform much better than QzSimple2.

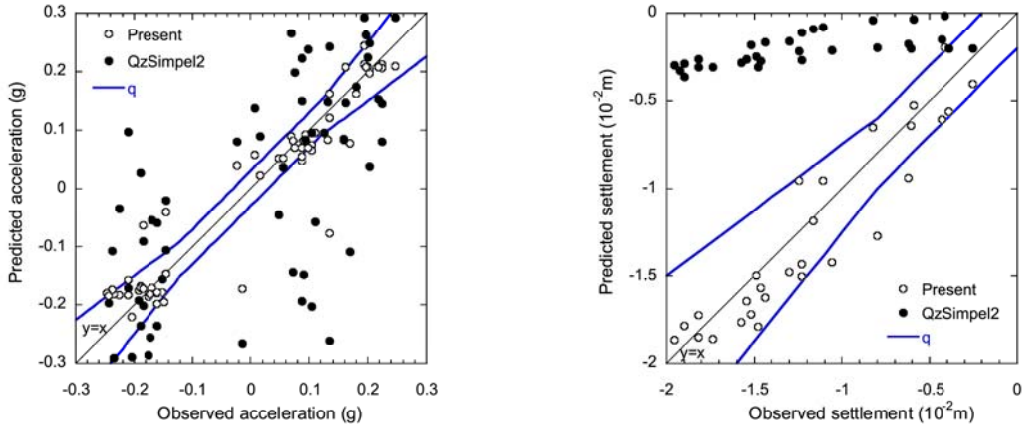

(a) Acceleration response of bridge deck **(b) Settlement-rotation response of foundation**

Fig. A4. Scatter plots for comparison between the Winkler model and the experiments for the 0.15 g acceleration amplitude.

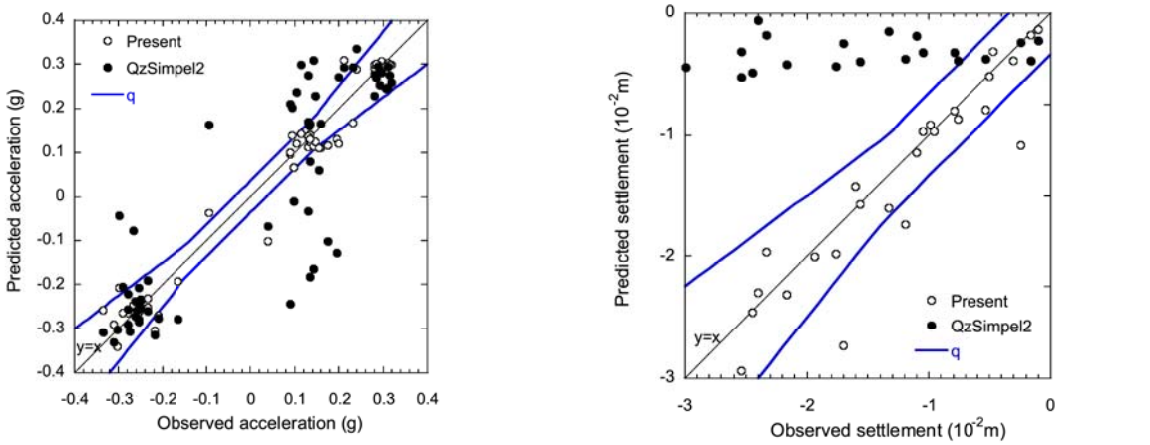

(a) Acceleration response of bridge deck **(b) Settlement-rotation response of foundation**

Fig. A5. Scatter plots for comparison between the Winkler model and the experiments for the 0.50 g acceleration amplitude.

References

[1] Harukigaoka Wind Power Co., Ltd, 2018. Accident survey report, 2018. (In Japanese) (https://www.meti.go.jp/shingikai/sankoshin/hoan_shohi/denryoku_anzen/newenergy_hatsuden_wg/pdf/009_05_00.pdf).

[2] Butt UA, Ishihara T. Seismic load evaluation of wind turbine support structures considering low structural damping and soil structure interaction. Proc EWEA2012 2012:1–9.

[3] Wang L, Ishihara T. A study of the effects of foundation uplift on the seismic loading of wind turbine tower and shallow foundation using a new dynamic Winkler model. Eng Struct 2020;219:110745.

[4] DNVGL-ST-0126. Support structures for wind turbines. Oslo, Norway: DNV; 2016.

[5] Ishihara T. Guidelines for Design of Wind Turbine Support Structures and Foundations, 2010. (In Japanese).

[6] Zhang Y, Andersen KH. Scaling of lateral pile py response in clay from laboratory stress-strain curves. Mar Struct 2017;53:124–35.

[7] Wang L, Lai Y, Hong Y, Mašín D. A unified lateral soil reaction model for monopiles in soft clay considering various length-to-diameter (L/D) ratios. Ocean Eng 2020;212:107492.

[8] Lai Y, Wang L, Zhang Y, Hong Y. Site-specific soil reaction model for monopiles in soft clay based on laboratory element stress-strain curves. Ocean Eng 2021;220:108437.

[9] Zhang Y, Aamodt KK, Kaynia AM. Hysteretic damping model for laterally loaded piles. Mar Struct 2021;76:102896.

[10] Cheng XL, El Naggar MH, Lu DC, Wang PG, Tu WB. A cyclic p-y elastoplastic model applied to lateral loaded pile in soft clays[J]. Can Geotech J 2022;60(6):885–901.

[11] Wang L, Ishihara T. New p-y model for seismic loading prediction of pile foundations in non-liquefiable and liquefiable soils considering modulus reduction and damping curves. Soils Found 2022;62(5):101201.

[12] Raychowdhury P, Hutchinson TC. Performance evaluation of a nonlinear Winkler-based shallow foundation model using centrifuge test results. Earthq Eng Struct Dyn 2009;38(5):679–98.

[13] Wang L, Ishihara T. A study of the effects of foundation uplift on the seismic loading of wind turbine tower and shallow foundation using a new dynamic Winkler model. Eng Struct 2020;219:110745.

[14] Allotey N, El Naggar MH. Analytical moment–rotation curves for rigid foundations based on a Winkler model. Soil Dyn Earthq Eng 2003;23(5):367–81.

[15] Allotey N, El Naggar MH. Generalized dynamic Winkler model for nonlinear soil–structure interaction analysis. Can Geotech J 2008;45(4):560–73.

[16] Allotey N, El Naggar MH. An investigation into the Winkler modeling of the cyclic response of rigid footings. Soil Dyn Earthq Eng 2008;28(1):44–57.

[17] Bazeos N, Hatzigeorgiou GD, Hondros ID, Karamaneas H, Karabalis DL, Beskos DE. Static, seismic and stability analyses of a prototype wind turbine steel tower. Eng Struct 2002;24:1015–25.

[18] Witcher D. Seismic analysis of wind turbines in the time domain. Wind Energy 2005;8(1):81–91.

[19] Song B, Yi Y, Wu JC. Study on seismic dynamic response of offshore wind turbine tower with monopile foundation based on M method. Adv Mater Res 2013;663:686–91.

[20] Kim WS, Jeoung C, Lee KM, Lee JH. Seismic analysis of concrete conical foundation for 5 MW wind turbine. Adv Mater Res 2013;831:133–6.

[21] Liang F, Yuan Z, Liang X, Zhang H. Seismic response of monopile-supported offshore wind turbines under combined wind, wave and hydrodynamic loads at scoured sites. Comput Geotech 2022;144:104640.

[22] Huang Y, Zhao M, Wang P, Cheng X, Du X. Analytical solution of dynamic responses of offshore wind turbine supported by monopile under combined earthquake, wave and wind. Ocean Eng 2023;267:113319.

[23] Alkhoury P, Soubra AH, Rey V, Aït-Ahmed M. Dynamic analysis of a monopile-supported offshore wind turbine considering the soil-foundation-structure interaction. Soil Dyn Earthq Eng 2022;158:107281.
[24] Kiyomiya O, Rikiji T, van GELDER PH. Dynamic response analysis of onshore wind energy power units during earthquakes and wind. The Twelfth International Offshore and Polar Engineering Conference. OnePetro; 2002 May 26.
[25] Mensah A.F., Duenas-Osorio L., Prowell I., Asareh M.A. Probabilistic combination of earthquake and operational loads for wind turbines. In Proceedings of the 15th World Conference of Earthquake Engineering. Lisboa, Portugal, 2012.
[26] Pérez Rocha LE, López López A, Maldonado Limenéz D, Manjarrez Garduño LE, de León E. Reliability index for wind turbines subjected to wind and seismic actions. In: Strauss A, Frangopol D, Bergmeister K, editors. In Life-cycle and sustainability of civil infrastructures system. Boca Raton, FL, USA: CPC Press/Taylor & Francis; 2013.
[27] Nuta E, Christopoulos C, Packer JA. Methodology for seismic risk assessment for tubular steel wind turbine towers: application to Canadian seismic environment. Can J Civ Eng 2011;38:293–304.
[28] El Haj AK, Soubra AH, Fajoui J. Probabilistic analysis of an offshore monopile foundation taking into account the soil spatial variability. Comput Geotech 2019; 106:205–16.
[29] Prowell I, Veletzos M, Elgamal A, Restrepo J. Experimental and numerical seismic response of a 65 kW wind turbine. J Earthq Eng 2009;13(8):1172–90.
[30] Zhao B, Cui T, Xu Z, Cao Y. Experimental study on seismic behaviour and vibration control of wind turbine and electrical transmission tower. In: Klinkel S, Butenweg C, Lin G, Holtschoppen B, editors. Seismic Design of Industrial Facilities. Germany: Springer Fachmedien Wiesbaden; 2014.
[31] Lauffer JP, Carne TG, Ashwill TD. Modal testing in the design evaluation of wind turbines. Rep. No. SAND87- 2461. Albuquerque, NM, USA: Sandia, National Laboratories,; 1988.
[32] Adams D, White J, Rumsey M, Farrar C. Structural health monitoring of wind turbines: method and application to a HAWT. Wind Energy 2011;14:603–23.
[33] Sim HB, Prowell I, Elgamal A, Uang CM. Flexural tests and associated study of a full-scale 65-kW wind turbine tower. J Struct Eng 2014;140(5):04013110.
[34] Cheng XL, El Naggar MH, Lu DC, Wang PG, Tu WB. A cyclic p-y elastoplastic model applied to lateral loaded pile in soft clays. Can Geotech J 2022;60(6):885–901.
[35] Cheng X, Li M, Ma C, El Naggar MH, Wang P, Sun X. Dynamic analysis of tripod pile foundation in clays for offshore wind turbines. Ocean Eng 2023;287:115832.
[36] Wang P, Lu H, Wang M, Nagarajaiah S, Du X. Experimental and numerical investigations on seismic responses of wind turbine structures with amplifying damping transfer system. Soil Dyn Earthq Eng 2023;175:108277.
[37] Cheng XL, Li Y, Mu K, El Naggar MH, Zhou Y, Wang P, et al. Seismic response of tripod suction bucket foundation for offshore wind turbine in sands. Soil Dyn Earthq Eng 2024;177:108353.
[38] Wang P, Yu W, Zhao M, Du X. Effects of wind-wave-current-earthquake interaction on the wave height and hydrodynamic pressure based on CFD method. Ocean Eng 2024;305:117909.
[39] Wang P, Huang Y, Zhao M, Cheng X, Du X. Analytical solution for simplifying the pile-soil interaction to a spring-damping system under horizontal vibration. Soils Found 2024;64(3):101469.
[40] Katsanos EI, Thöns S, Georgakis C. Wind turbines and seismic hazard: a state-of-the-art review. Wind Energy 2016;19(11):2113–33.
[41] Valamanesh V, Myers AT. Aerodynamic damping and seismic response of horizontal axis wind turbine towers. J Struct Eng 2014;140(11):04014090.
[42] Mazzoni S, McKenna F, Scott MH, Fenves GL. OpenSees command language manual. Pac Earthq Eng Res (PEER) Cent 2006;264:137–58.
[43] Nguyen BN, Tran NX, Han JT, Kim SR. Evaluation of the dynamic p–yp loops of pile-supported structures on sloping ground. Bull Earthq Eng 2018;16(12): 5821–42.
[44] Ishihara K, Yoshida N, Tsujino S. Modelling of stress-strain relations of soils in cyclic loading. Int Conf Numer Methods Geomech 1985.
[45] Wilson DW. Soil-pile-superstructure interaction in liquefying sand and soft clay. America: University of California, Davis; 1998.
[46] Turner B. Kinematic Pile-soil interaction in liquefied and nonliquefied ground. LosAngles: University of California; 2016.
[47] Oh S, Ishihara T. Structural parameter identification of a 2.4 MW bottom fixed wind turbine by excitation test using active mass damper. Wind Energy 2018;21 (11):1232–8.
[48] Pile foundation design manual. Japan Road Association; 2020.
[49] Nagai T, Nakamura T, Nagano K. Damage evaluation of pile foundations by high-frequency impact elastic wave method. Proceeding of Technology Forum 2013. Japan Geotechnical Consultants Association; 2013.
[50] Anastasopoulos I, Loli M, Georgarakos T, Drosos V. Shaking table testing of rocking-isolated bridge pier on sand. J Earthq Eng 2013;17(1):1–32.
[51] Anastasopoulos I, Georgarakos T, Georgiannou V, Drosos V, Kourkoulis R. Seismic performance of bar-mat reinforced-soil retaining wall: Shaking table testing versus numerical analysis with modified kinematic hardening constitutive model. Soil Dyn Earthq Eng 2010;30(10):1089–105.
[52] Ishihara T, Wang L. A study of modal damping for offshore wind turbines considering soil properties and foundation types. Wind Energy 2019;22(12): 1760–78.
[53] Schatzmann M, Olesen HR, Franke J. COST 732 model evaluation case studies: approach and results. Brussels: COST Office; 2010. p. 121.
[54] Oettl D. Quality assurance of the prognostic, microscale wind-field model GRAL 14.8 using wind-tunnel data provided by the German VDI guideline 3783-9. J Wind Eng Ind Aerodyn 2015;142:104–10.